



# Coordinated NanoSIMS and FIB-TEM analyses of organic matter and associated matrix materials in CR3 chondrites

Christine Floss<sup>a,\*</sup>, Corentin Le Guillou<sup>b,c</sup>, Adrian Brearley<sup>b</sup>

<sup>a</sup> *Laboratory for Space Sciences and Physics Department, Washington University, One Brookings Drive, St. Louis, MO 63130, USA*

<sup>b</sup> *Department of Earth and Planetary Sciences, MCS03-2040, University of New Mexico, Albuquerque, NM 87106, USA*

<sup>c</sup> *Institut für Geologie, Mineralogie und Geophysik, Ruhr-Universität Bochum, 44780 Bochum, Germany*

Received 5 October 2013; accepted in revised form 17 April 2014; Available online 5 May 2014

## Abstract

The organic matter in the primitive CR3 chondrites QUE 99177 and MET 00426 exhibits, as in other CR chondrites, N isotopic compositions characterized by large enrichments in <sup>15</sup>N compared to solar. These enrichments are present in the matrices of these two meteorites as localized hotspots associated with C-rich grains, and larger, more diffuse regions with more modest enrichments in <sup>15</sup>N. Occasionally depletions in <sup>15</sup>N are also observed. FIB-TEM analysis of isotopically anomalous as well as isotopically normal C-rich grains from the matrix of MET 00426 shows that both types of grains consist of highly disordered organic matter that exhibits a variety of morphologies. There are no obvious correlations of isotopic composition with morphology, petrographic association or elemental composition. Large diffuse regions with modest <sup>15</sup>N enrichments may be the result of fluid action that redistributed organic matter (and the associated <sup>15</sup>N enrichments) in veins and cracks along grain boundaries. Grain formation likely occurred in a variety of environments (e.g., molecular clouds or the outer regions of the protosolar nebula) via UV photolysis of simpler precursor ices with variable isotopic compositions.

© 2014 Elsevier Ltd. All rights reserved.

## 1. INTRODUCTION

Presolar materials consist of both circumstellar grains that formed around evolved stars and in supernova ejecta, and grains and organic matter that formed in cold interstellar or protosolar environments. Small amounts of both types of materials survived the collapse of the molecular cloud from which our solar system originated and were incorporated into the primitive meteorites, interplanetary dust particles (IDPs) and Antarctic micrometeorites (AMMs) in which we find them today. A relatively small fraction of the organic matter (OM) in IDPs and primitive

meteorites exhibits C isotopic anomalies (e.g., Floss et al., 2004, 2006; Busemann et al., 2006), and is typically also anomalous in N. Other OM, characterized by N and/or H isotopic anomalies but without C isotopic anomalies, is much more abundant and is also commonly found in IDPs and primitive meteorites (Aléon et al., 2001, 2003; Messenger et al., 2003; Busemann et al., 2006, 2009; Floss et al., 2006, 2010; Hashizume et al., 2011). These light element isotopic anomalies are traditionally thought to have formed via low temperature ion–molecule reactions, either in the interstellar medium (e.g., Messenger and Walker, 1997) or the protosolar nebula (e.g., Remusat et al., 2006, 2009, 2010; Gourier et al., 2008; Aléon, 2010). Further isotopic evolution may also have occurred in asteroidal parent bodies (e.g., Alexander et al., 2010; Herd et al., 2012; Le Guillou et al., in press).

\* Corresponding author. Tel.: +1 3149356206.  
E-mail address: [floss@wustl.edu](mailto:floss@wustl.edu) (C. Floss).

CR chondrites are relatively abundant among carbonaceous chondrite groups and, among other characteristics, are noted for the presence of primitive insoluble organic matter (IOM) with localized isotopic anomalies in H, C and N (e.g., Busemann et al., 2006). Many CR chondrites have experienced aqueous alteration, leading to hydration of matrix material (Krot et al., 2002), and subsequent destruction of presolar silicates and oxides (Nagashima et al., 2004; Floss and Stadermann, 2005). However, more recent studies have also identified CR chondrites that are significantly less altered than most members of this group. QUE 99177 and MET 00426 are two CR3 chondrites whose matrices contain few phyllosilicates and instead are dominated by amorphous silicates (Abreu and Brearley, 2010; Le Guillou and Brearley, 2013) similar to those found in other primitive carbonaceous chondrites with high abundances of presolar grains, such as ALHA77307 or Acfer 094 (Brearley, 1993; Greshake, 1997). The carbonaceous matter of these two CR3 chondrites has escaped significant thermal processing, and consists, as in other CRs, of small aromatic units and aliphatic chains (Cody and Alexander, 2005; Derenne and Robert, 2010; Le Guillou et al., 2012) with detectable concentrations of elements such as N, O and S, which are usually lost as a result of secondary processing such as parent body metamorphism (Alexander et al., 2007; Abreu and Brearley, 2010; Le Guillou and Brearley, 2013; Le Guillou et al., in press). High amino acid contents indicate, further, that the soluble organic matter in these type 3.0 CR chondrites is also very primitive (Martins et al., 2008; Glavin et al., 2011).

NanoSIMS ion imaging studies of these two meteorites show that both contain abundant presolar grains of circumstellar origin, including silicates, oxides and SiC (Floss and Stadermann, 2009a,b; Nguyen et al., 2010). Like other CR chondrites, QUE 99177 and MET 00426 contain carbonaceous matter with anomalous N isotopic compositions. In addition, abundant C isotopic anomalies are found in the IOM of these meteorites (Floss and Stadermann, 2009b). The presence of this material in these primitive CR3 chondrites is of significance because of the relative scarcity of such material compared to the abundant H and N isotopic anomalies in much extraterrestrial organic matter, and suggests that secondary processes are probably important in accounting for this scarcity (Floss and Stadermann, 2009b).

We have carried out coordinated NanoSIMS, Auger and FIB-TEM analyses of the C- and/or N-anomalous phases in the CR3 chondrites QUE 99177 and MET 00426. Our investigation of the compositions, morphologies and petrographic associations of this material provides constraints on its origin(s) and insights into how it is affected by secondary processing. Preliminary results have been previously reported (Floss and Stadermann, 2009c; Le Guillou et al., 2010; Floss et al., 2011).

## 2. EXPERIMENTAL

We studied one polished thin section of each meteorite (QUE 99177,26 and MET 00426,24), obtained from the Curation Facility at Johnson Space Center (JSC). Thin section preparation at JSC follows a standard protocol in

which samples are impregnated with epoxy, cut with a diamond saw and polished in multiple steps with SiC and diamond paste. Harrington and Righter (2013) provide detailed information on the preparation procedure for carbonaceous chondrites, which require extra care due to the fragility of their components. The sections were initially documented with an Olympus BH2 optical microscope and candidate matrix areas were identified for presolar grain searches.

We used the Washington University Cameca NanoSIMS 50 ion microprobe to identify isotopically anomalous regions in matrix-rich areas of the two meteorites. The measurements were carried out by rastering a  $\sim 1$  pA  $\text{Cs}^+$  primary ion beam over individual matrix areas and collecting secondary ions of C ( $^{12}\text{C}^-$  and  $^{13}\text{C}^-$ ), N (measured as the  $\text{CN}^-$  molecule:  $^{12}\text{C}^{14}\text{N}^-$  and  $^{12}\text{C}^{15}\text{N}^-$ ) and Si ( $^{28}\text{Si}^-$ ), along with secondary electrons (SE). Areas of  $12 \times 12 \mu\text{m}^2$  were pre-sputtered using a high primary beam current ( $\sim 10$  pA) to remove the carbon coating and implant  $\text{Cs}^+$ , after which  $10 \times 10 \mu\text{m}^2$  regions within these areas were analyzed. The measurements consisted of multiple scans (typically 5, with dwell times of 20 ms/px) that were added together to constitute single image measurements of  $256^2$  pixels. The analyses were carried out in automated mapping mode, with automatic stage movement to subsequent matrix areas following a predefined grid pattern. Carbon isotopic compositions were normalized to the average composition of the matrix material from each meteorite, assuming normal ( $^{12}\text{C}/^{13}\text{C} = 90$ ) bulk isotopic compositions (e.g., Alexander et al., 2007). Nitrogen isotopic compositions were normalized to a standard consisting of a mixture of synthetic SiC and  $\text{Si}_3\text{N}_4$  ( $^{14}\text{N}/^{15}\text{N} = 272$ ). The total areas mapped were  $7300 \mu\text{m}^2$  for QUE 99177 and  $7100 \mu\text{m}^2$  for MET 00426. Isotope ratio images were calculated following corrections for outliers and stage drift; areas shown in gray in the figures indicate regions in which count rates were too low to determine statistically meaningful isotopic ratios (e.g., Stadermann et al., 2005). Isotopic compositions are considered anomalous if they differ by more than  $5\sigma$  from normal and are present in at least 3 consecutive layers.

Following NanoSIMS analyses, Auger elemental spectra were obtained with the Washington University PHI 700 Auger Nanoprobe. Regions of interest were briefly sputter-cleaned with a defocused 2 kV  $1 \mu\text{A}$   $\text{Ar}^+$  ion beam to remove atmospheric surface contamination. Auger electron energy spectra were obtained from 30 to 1730 eV with a 10 kV 0.25 nA primary electron beam which was rastered over the grains of interest. Multiple scans of individual grains were added together to obtain Auger spectra, which were differentiated using a 7-point Savitsky–Golay smoothing and differentiation routine prior to peak identification and quantification. Carbon and N sensitivity factors were obtained by least-squares fitting of the Auger intensities to the C abundances and N/C ratios of a set of terrestrial kerogen standards (Floss et al., 2010); C concentrations in the kerogens ranged from 64 to 77 wt.% and N/C ratios varied between 0.002 and 0.021 (Hayes et al., 1983). Detection limits depend on a variety of analytical factors, but are typically on the order of 3 at.% or less. See Stadermann

et al. (2009) for more detailed information about the use of Auger spectroscopy for cosmochemical applications.

Selected carbonaceous grains were targeted for focused ion beam (FIB) lift-out and TEM analysis. When feasible, the profiles for the lift-outs included both isotopically anomalous (C and/or N) and isotopically normal grains. The sections were made with the FEI Quanta 3D FEG/SEM/FIB instrument at the University of New Mexico, equipped with an EDAX Apollo 40 SDD EDS system and an Omniprobe 200 micromanipulator. Samples for lift-out were prepared by initially using the electron beam to deposit W fiducial markers over the grains of interest for subsequent identification, followed by deposition of a  $2 \text{ (h)} \times 2 \text{ (w)} \mu\text{m}$  Pt layer from 8 to 25  $\mu\text{m}$  in length, for protection from damage during ion milling. The samples were removed from the thin section and transferred to Cu TEM half grids, after which they were milled to electron transparency using a 30 kV Ga ion beam operated at beam currents of 3 nA to 10 pA, with a progressive reduction in beam current as the sample became thinner.

The TEM analyses were carried out with the University of New Mexico's JEOL 2010F FEG-TEM scanning transmission electron microscope fitted with a GATAN 2000 image filtering system. Energy dispersive X-ray spectroscopy (EDS) analyses were obtained with an Oxford INCA 200 system using an ultra-thin window Pentafet detector. Additional information on the TEM analyses is provided by Le Guillou and Brearley (2013).

Following TEM analysis, the FIB sections were re-analyzed in the NanoSIMS, to confirm the anomalies in the original surface grains and to obtain data for the rest of the section. The analysis and data processing protocols were similar to those used in the original C and N imaging measurements, except that we used a shorter dwell time (5 ms/px) and acquired more scans (between 75 and 150) for each image measurement, in order to more effectively monitor changes in the FIB section during the analysis. The sizes of the raster areas ranged between  $7 \times 7 \mu\text{m}^2$  and  $11 \times 11 \mu\text{m}^2$ , depending on the size of the FIB section. In one section (5b-6) only C isotopes were measured.

### 3. RESULTS

#### 3.1. Isotopic and elemental compositions

Tables A1 and A2 in the Appendix list the N and C isotopic compositions of each of the  $10 \times 10 \mu\text{m}^2$  areas measured in QUE 99177 and MET 00426, respectively.

Also listed are the N and C isotopic compositions of localized isotopically anomalous hotspots within these areas. Carbon isotopic compositions in the matrix areas are normal, but average N isotopic compositions in the  $10 \times 10 \mu\text{m}^2$  areas are typically enriched in  $^{15}\text{N}$ , with  $\delta^{15}\text{N}$  up to  $\sim 500\text{‰}$  (Table 1). The mean N isotopic composition of all areas measured in QUE 99177 is somewhat more  $^{15}\text{N}$ -rich than that in MET 00426 ( $^{14}\text{N}/^{15}\text{N} = 229 \pm 16$  vs.  $248 \pm 22$ ; Table 1). Most localized hotspots are  $^{15}\text{N}$ -enriched, with  $\delta^{15}\text{N}$  up to  $\sim 2500\text{‰}$ , but some  $^{15}\text{N}$ -depleted 'coldspots' are also observed (Fig. 1). Most of the N isotopic anomalies reported here are not accompanied by C isotopic anomalies. However, as noted earlier, both QUE 99177 and MET 00426 also contain carbonaceous grains with  $^{13}\text{C}$ -enriched and  $^{13}\text{C}$ -depleted compositions (Floss and Stadermann, 2009b); those with available N data are also listed in Tables A1 and A2, and are marked with an asterisk.

Tables A1 and A2 also list the  $\text{CN}^-/\text{C}^-$  ratios of the matrix areas and hotspots analyzed in QUE 99177 and MET 00426.  $\text{CN}^-/\text{C}^-$  ratios for the matrix areas range from 0.36 to 2.21, with most falling between 0.5 and 1.5. Fig. 2 shows  $\text{CN}^-/\text{C}^-$  ratios plotted against N isotopic compositions for both the matrix areas and localized hotspots. The matrix areas can be divided into three sub-populations: a main group that shows a general increase in  $^{15}\text{N}$  with increasing  $\text{CN}^-/\text{C}^-$ , another group with more strongly elevated  $^{15}\text{N}$  enrichments at intermediate  $\text{CN}^-/\text{C}^-$  ratios and a third group with higher  $\text{CN}^-/\text{C}^-$  ratios and lower  $^{15}\text{N}$  values (Fig. 2a). The latter consist almost entirely of measurements from a single matrix region in MET 00426; other areas analyzed in this matrix region have somewhat lower  $\text{CN}^-/\text{C}^-$  ratios, but also show little enrichment of  $^{15}\text{N}$ . Individual hotspots within the matrix areas of QUE 99177 and MET 00426 show a larger range of  $\text{CN}^-/\text{C}^-$  ratios, up to  $\sim 7$  (Fig. 2b). The  $\text{CN}^-/\text{C}^-$  ratios of the hotspots show no obvious trend with N isotopic composition: hotspots with depletions in  $^{15}\text{N}$  show a similar range of ratios as those with enrichments.

We used Auger spectroscopy to examine the isotopically anomalous areas in more detail. Fig. 3 shows the range of morphologies observed for carbonaceous material in the matrix of QUE 99177. Whereas many of the grains are irregular in shape (Fig. 3a, e, f), others are smooth and rounded (Fig. 3b and d) like nanoglobules identified in other studies (e.g., Nakamura-Messenger et al., 2006; Garvie et al., 2008; De Gregorio et al., 2013; Hashigushi et al., 2013). Sizes are typically on the order of a few

Table 1  
Nitrogen and C isotopic compositions in matrix from QUE 99177 and MET 00426.

Sample	$^{14}\text{N}/^{15}\text{N}$	$\delta^{15}\text{N}$ (‰)	$^{12}\text{C}/^{13}\text{C}$	$\delta^{13}\text{C}$ (‰)	$\text{CNN}^-/\text{C}^-$
QUE 99177 (mean)	$229 \pm 16$	$194 \pm 88$	$90.0 \pm 0.7$	$0 \pm 7$	
Matrix range <sup>1</sup>	181–264	29–502	88.8–92.7	–29 to 14	0.36–1.93
Hotspots range	79–421	–354 to 2460	80.5–120.9	–256 to 118	0.34–6.94
MET 00426 (mean)	$248 \pm 22$	$105 \pm 108$	$90.0 \pm 0.9$	$0 \pm 10$	
Matrix range <sup>1</sup>	188–278	–22 to 443	86.9–92.0	–22 to 35	0.38–2.21
Hotspots range	85–430	–367 to 2201	76.0–106.7	–156 to 184	0.30–4.89

<sup>1</sup> Values obtained on individual  $10 \times 10 \mu\text{m}$  areas.

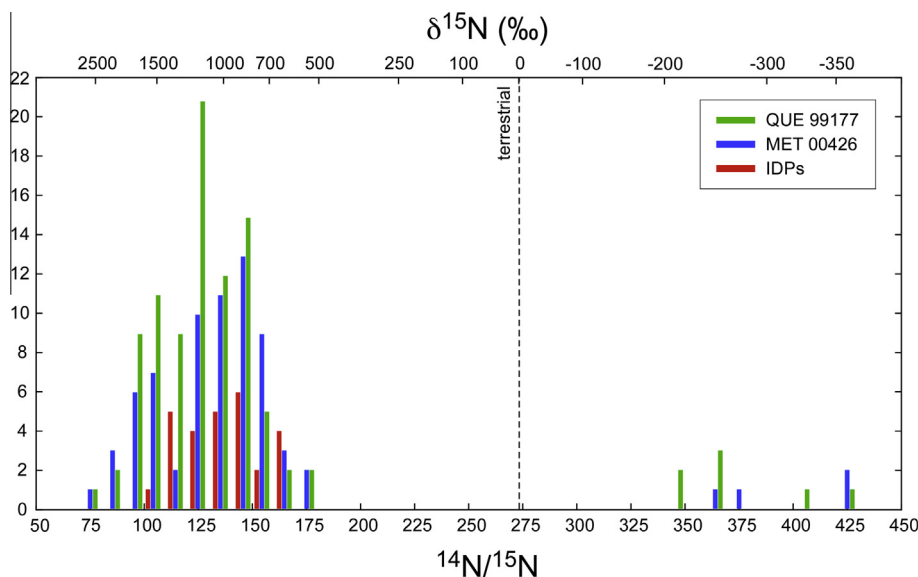


Fig. 1. Distribution of N isotopic compositions in isotopically anomalous hotspots from QUE 99177 and MET 00426. Also shown are data for primitive anhydrous IDPs (Floss et al., 2006; Busemann et al., 2009).

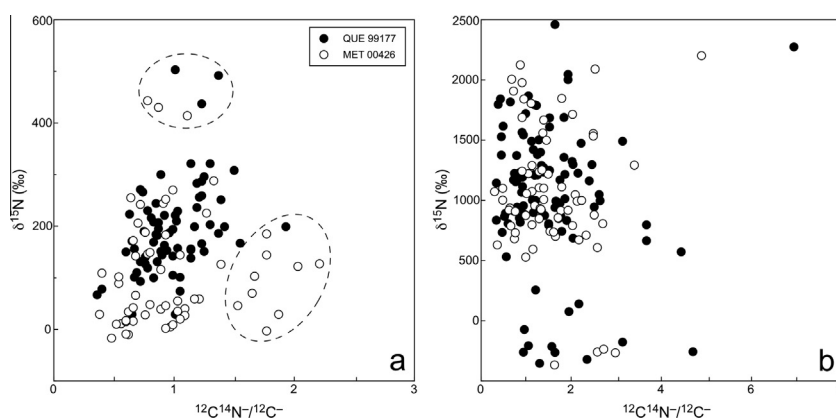


Fig. 2. Nitrogen isotopic compositions (expressed as permil deviations from the terrestrial value) vs.  $CN^-/C^-$  ratios in (a)  $10 \times 10 \mu m^2$  matrix areas and (b) individual localized hotspots from QUE 99177 and MET 00426. The dashed lines in (a) show two sub-sets of matrix areas that fall off of the main trend of greater enrichment in  $^{15}N$  with higher  $CN^-/C^-$ .

hundred nanometers up to about a micrometer in size. In addition to such compact grains, carbonaceous matter is also present as aggregates with highly irregular shapes that are up to several micrometers in size (Fig. 3c). In some cases, C-rich veins or cracks extend from the carbonaceous grains (Fig. 3e). Auger spectra were obtained from a number of C-rich regions with variable N isotopic compositions (Table 2). The spectra typically are dominated by C and O, but can also contain minor N and/or S. Some carbonaceous regions also show the presence of Fe and, in a few cases, Mg or Si (Table 2). These areas generally also contain higher abundances of O, some of which can probably be attributed to the presence of other phases, such as silicates or oxides, embedded in the carbonaceous matter (e.g., Fig. 3a and e). In contrast, S abundances in the carbonaceous regions are not correlated with the presence of Fe (Table 2), suggesting that the S is intrinsic to the carbonaceous matter and also

that Fe, when present, is probably hosted in either silicates or oxides. Nitrogen is below detection in most of the carbonaceous grains. Where present, the N/C ratios are relatively uniform, ranging from 0.02 to 0.03 (Table 2). Sulfur abundances are more variable, with concentrations between 1–6 at.% and S/C ratios that vary by more than a factor of 5.

### 3.2. FIB-TEM analyses

In order to understand the structures and petrographic associations of isotopically anomalous grains in more detail, we created FIB-liftout sections of several C- and/or N-anomalous areas in MET 00426 and examined them in the TEM. Following the TEM analyses, we returned the sections to the NanoSIMS for isotope imaging. In general, our observations showed that, despite the primitive

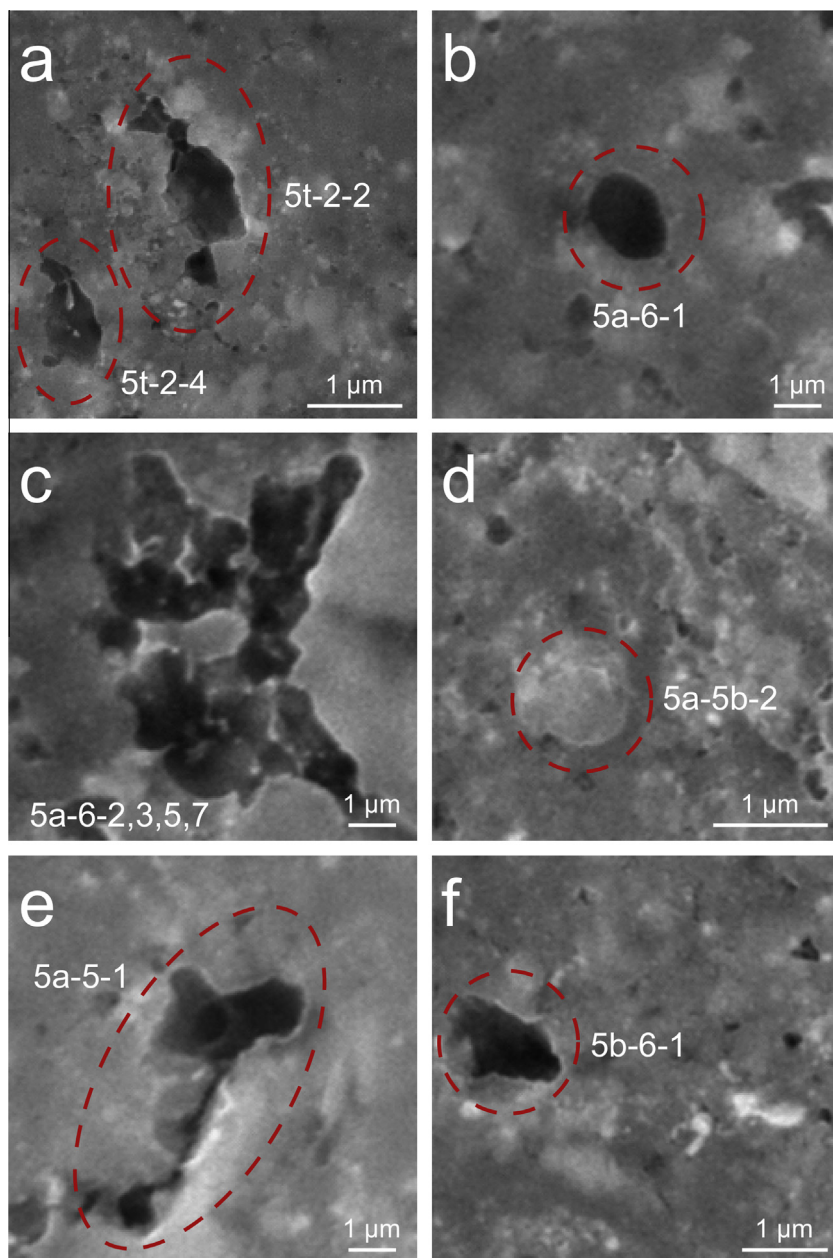


Fig. 3. Secondary electron images of carbonaceous regions in QUE 99177: (a) irregular regions associated with mineral inclusions; (b) smooth round grain; (c) irregular aggregate; (d) smooth round region; (e) irregular region with hole and vein extending into matrix; (f) irregular grain. Numerical designations correspond to Auger analyses presented in Table 2.

nature of MET 00426, phyllosilicates are present in the matrix, although they are quite heterogeneously distributed. They are typically intermingled at a scale of a few hundreds of nanometers with amorphous silicates, which also show evidence of hydration. The compositions of both the phyllosilicates and the amorphous silicates are intermediate between saponite and serpentine, and their water contents are estimated to be around 8–10 wt.% (Le Guillou and Brearley, 2013). All of the C-rich grains analyzed, whether they are isotopically normal or exhibit anomalous C and/or N isotopic compositions, are disordered and are similar to those described in type 1 and 2 chondrites (Garvie et al.,

2008; Le Guillou et al., 2012). Energy-filtered TEM maps and EDS analyses shows that most of the OM is compositionally similar, typically with O and S present, but N below detection limits (see also Le Guillou and Brearley, 2013). Detailed observations for each section are presented below.

*Area 5b-6:* C and N imaging of matrix area 5b-6 revealed the presence of a C-rich grain enriched in  $^{13}\text{C}$  and  $^{15}\text{N}$  ( $\delta^{13}\text{C} = 140 \pm 15\text{‰}$ ;  $\delta^{15}\text{N} = 630 \pm 75\text{‰}$ ; Floss and Stadermann, 2009b). Its round, hollow appearance suggested that it was a nanoglobule but, in the absence of structural data, graphite could not be ruled out (Floss

Table 2  
Elemental compositions of C-rich regions in QUE 99177 matrix.

Sample	$\delta^{15}\text{N}$ (‰)	Size (nm)	C	N	O	S	N/C	S/C	Other elements
5a-4-2	606 ± 29	750	86.1		12.0	1.9		0.022	Some Fe
5a-4-3	268 ± 22	1000 × 600	86.8	1.9	9.9	1.4	0.022	0.016	
5a-4-4	557 ± 29	1250 × 500	86.7		7.1	6.2		0.071	
5a-4-7	725 ± 27	600	82.5	1.6	14.2	1.7	0.019	0.021	Some Fe
5a-5-1	417 ± 30	750 × 250	89.6		7.8	2.6		0.029	
5a-5-2	572 ± 34	500 × 250	88.3		9.5	2.1		0.024	
5a-5b-1	1162 ± 71	600 × 400	89.6		8.6	1.8		0.020	
5a-5b-2	10 ± 43	600	87.9		12.1				
5a-6-1	744 ± 57	500 × 250	88.2		9.8	1.9		0.022	
5a-6-2 <sup>1</sup>	458 ± 24	1700 × 1000	83.7		14.8	1.5		0.018	Some Fe
5a-6-3 <sup>1</sup>	631 ± 25	1700 × 1000	87.2		11.7	1.1		0.013	Minor Fe
5a-6-5 <sup>1</sup>	525 ± 24	1700 × 1000	82.1		15.1	2.7		0.033	Some Fe
5a-6-6	593 ± 32	250	78.0		18.5	3.4		0.044	Some Fe
5a-6-7 <sup>1</sup>	407 ± 22	1700 × 1000	80.2		17.0	2.8		0.036	Some Fe
5b-1-1	−149 ± 78	700 × 350	83.6	1.5	14.9		0.018		
5b-1-4 <sup>2</sup>	−266 ± 69	2000 × 750	88.9		11.1				
5b-1-5 <sup>2</sup>	−93 ± 83	2000 × 750	83.1		16.9				
5b-1-6 <sup>2</sup>	−318 ± 74	2000 × 750	88.4		11.6				
5b-1-7 <sup>2</sup>	−219 ± 86	2000 × 750	86.8	1.6	11.6		0.019		
5b-2-1	−66 ± 72	1000 × 750	89.5		10.5				
5b-6-1	557 ± 21	1350 × 550	77.0	2.4	14.5	6.1	0.031	0.079	
5b-6-2	893 ± 31	800	87.9		10.4	1.6		0.018	
5t-2-2	536 ± 22	2000 × 800	72.8	1.5	23.7	2.0	0.021	0.027	Fe, Mg, Si
5t-2-3	−19 ± 28	600	82.1		17.9				Some Fe, Mg
5t-2-4	633 ± 25	1000 × 500	74.8	1.7	21.9	1.6	0.023	0.021	Some Fe

<sup>1</sup> Part of a large aggregate grain with dimensions of  $1.7 \times 1.0 \mu\text{m}^2$ .

<sup>2</sup> Part of a large aggregate grain with dimensions of  $2.0 \times 0.75 \mu\text{m}^2$ .

and Stadermann, 2009b). A FIB section was cut through this grain and two other nearby, isotopically normal, C-rich grains (Fig. 4). TEM analysis of the anomalous grain, 5b-6c1, shows that it is not graphite, but rather consists of highly disordered organic matter, confirming its initial identification as the first nanoglobule with a C isotopic anomaly (e.g., Floss and Stadermann, 2009b). The grain is surrounded by Fe-rich amorphous silicates (Fig. 5a), typical for the matrix of this meteorite (Abreu and Brearley, 2010). The isotopically normal carbonaceous grains (Fig. 5b) also consist of highly disordered C and have compact morphologies; thin nano-veins filled with C extend into the interior of the section. A large, irregular C-rich region present at depth in the FIB section consists of aggregated nanoglobules in an ill-defined organic mass, and is associated with a large grain of tochilinite (Fig. 5c); amorphous silicates, phyllosilicates and sulfides are also present. Three Mg-rich crystalline silicate grains, whose (Mg + Fe)/Si ratios suggest that they are enstatite, are also present in the section (Figs. 4 and 5d). The C isotopic measurement of the section confirms the  $^{13}\text{C}$ -rich composition observed in the original measurement ( $^{12}\text{C}/^{13}\text{C} = 82 \pm 2$  vs.  $79 \pm 1$ ; Table 3); other carbonaceous areas in the section (including the two surface grains) have normal C isotopic compositions.

*Area 5b-9:* A FIB section was cut through a  $^{15}\text{N}$ -rich hotspot (Table 3) and another C-rich grain with a more

modest  $^{15}\text{N}$  enrichment (Fig. 6). The hotspot is a nanoglobule with a hollow center, while the other grain is a compact half-sphere. The nanoglobule is surrounded by hydrated amorphous silicates and nanophyllosilicates (Fig. 6d). The other grain is in contact with amorphous silicates, but also with an olivine grain connected to an Fe-sulfide (Fig. 6b). The section also contains an aggregate of large grains of enstatite ( $\sim 0.5$ – $1 \mu\text{m}$ ), which show signs of incipient aqueous alteration at their rims. Associated with this aggregate is an FeS grain, as well as two additional large areas ( $0.3$ – $1 \mu\text{m}$ ) of disordered carbonaceous matter (Fig. 6a). One of these is an aggregate of blocky grains (Fig. 6c). The other is also an aggregate of grains, which is connected to the nanoglobule by a vein of intermingled nanophyllosilicates and carbonaceous material (Fig. 6d and e). NanoSIMS C and N imaging confirmed that both of the original surface grains are enriched in  $^{15}\text{N}$  (Table 3), although the degree of  $^{15}\text{N}$  enrichment observed in the FIB section measurement of the hotspot is significantly less than the original value ( $\sim 500\text{‰}$  vs.  $\sim 1240\text{‰}$ ). One of the subsurface grain aggregates (C2) is also enriched in  $^{15}\text{N}$ , but the aggregate of grains associated with the nanoglobule (C3) has a normal N isotopic composition. Carbon isotopic compositions are normal throughout the section (Table 3).

*Area 1a-11:* This section was cut through a single  $^{15}\text{N}$ -rich hotspot with  $\delta^{15}\text{N} = 1160\text{‰}$  (Table 3). TEM

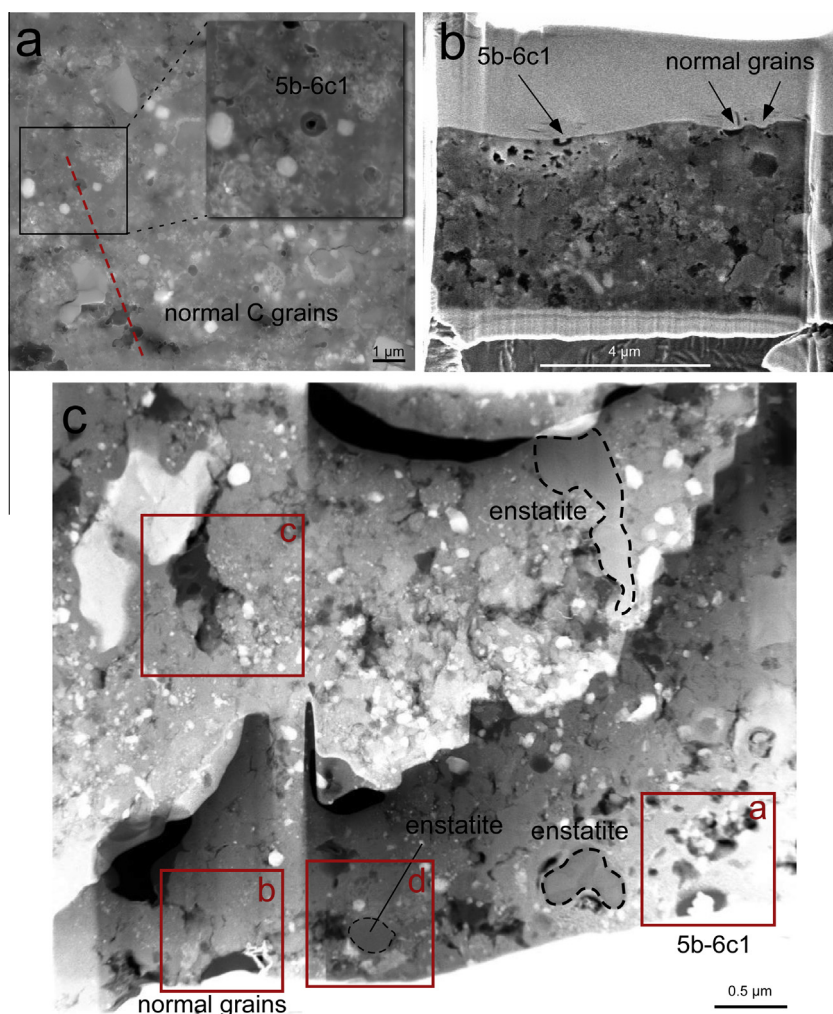


Fig. 4. MET 00426 matrix area 5b-6: (a) secondary electron image of area 5b-6, showing the line of the FIB cut; the inset shows C- and N-anomalous grain 5b-6c1; (b) secondary electron image of the FIB section during thinning; (c) dark field scanning transmission electron microscopy (DF-STEM) image of the FIB section. Boxes outline areas shown in Fig. 5.

analysis shows that it consists of a hollow nanoglobule attached to an irregularly-shaped grain (Fig. 7). NanoSIMS imaging of the FIB section confirms that the anomaly extends over both grains, albeit with a somewhat lower degree of  $^{15}\text{N}$  enrichment than the original hotspot (Table 3). The interior of the section contains a Ca-phosphate grain and coarser phyllosilicate domains than in other sections; the domains extend over several microns, indicating a more advanced degree of alteration. Overall, the section is relatively poor in carbonaceous matter; the isotopically anomalous grains are located in a less altered area containing amorphous silicates, nanophyllosilicates, and nanosulfides.

*Area 1a-15:* The FIB section was cut through a  $^{15}\text{N}$ -rich hotspot ( $\delta^{15}\text{N} = 1290\text{‰}$ ; Table A2) and an isotopically normal C-rich grain. The N-anomalous grain could not be re-located in the TEM, but the isotopically normal grain consists of an irregular aggregate of disordered carbonaceous grains (Fig. 8a). In addition, two adjacent nanoglobules are present at depth in the section and are in contact with sulfides and amorphous silicates (Fig. 8b).

The organic matter around them extends into boundaries between inorganic particles. NanoSIMS imaging indicates normal C and N isotopic compositions for both areas (Table 3).

*Area 1a-17:* TEM analysis of this  $^{15}\text{N}$ -rich hotspot shows that it consists of disordered C with a nanoglobule morphology (Fig. 9). The grain is in contact with amorphous silicates. This region of the matrix consists of a mixture of both more and less altered areas, occurring on the scale of a few micrometers. The less altered areas consist mainly of amorphous silicates, while the more altered areas contain phyllosilicates, fewer amorphous silicates, and nanosulfides with some porosity. Carbon-rich material is present throughout these altered areas of the section as small patches and veins (Fig. 9c). Nitrogen isotopic imaging confirms the  $^{15}\text{N}$  enrichment in the nanoglobule ( $\delta^{15}\text{N} = 690\text{‰}$ ; Table 3). In addition to this hotspot, other areas of the section are enriched in  $^{15}\text{N}$  at more modest levels (Fig. 9b; Table 3).

*Area 6d-2:* A FIB section was cut through a large area that is isotopically anomalous in both C and N, and a

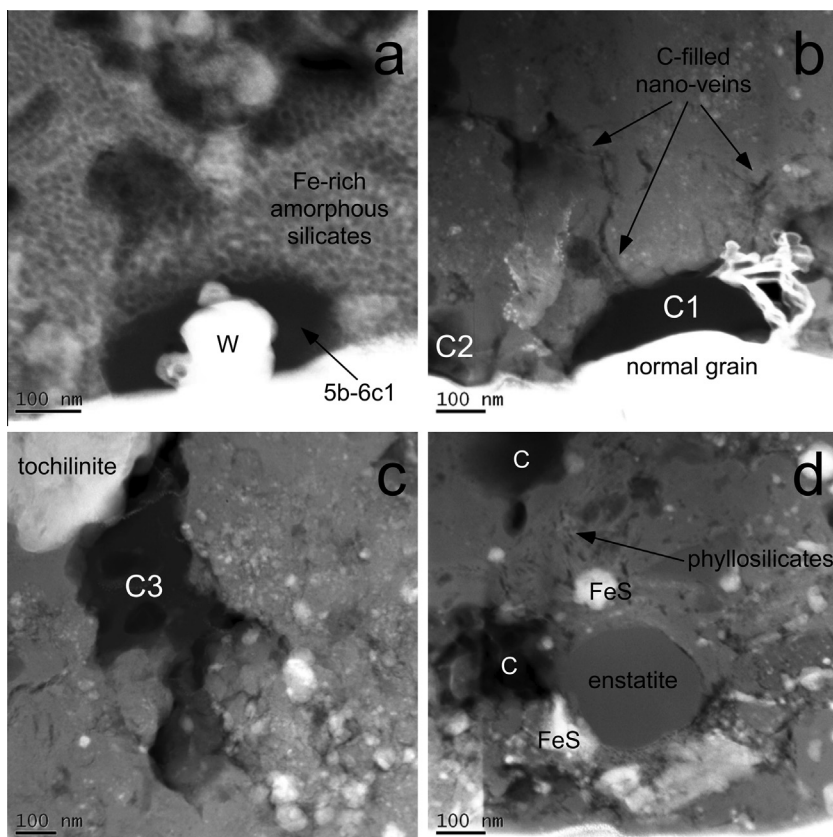


Fig. 5. Dark field STEM images of FIB section 5b-6 from MET 00426: (a) C- and N-anomalous grain 5b-6c1, surrounded by Fe-rich amorphous silicates; (b) isotopically normal grain; (c) irregularly-shaped region consisting of nanoglobules and other grains, associated with tochilinite; (d) enstatite associated with disordered C, sulfides (FeS) and phyllosilicates. Designations (5b-6c1, C1–C3) refer to NanoSIMS analyses presented in Table 3.

smaller isotopically normal grain (Fig. 10a). TEM analysis shows that the normal grain consists of compact disordered carbonaceous matter and is in contact with phyllosilicates and amorphous silicates, as well as an enstatite grain (Fig. 10c). The hotspot actually consists of two grains separated by a small amount of matrix material (Fig. 10b). Both are disordered C, but the morphologies of the grains are unusual, with a distinct structure. These grains are also associated with phyllosilicates, sulfides and a large olivine grain ( $\sim 1 \mu\text{m} \times 0.5 \mu\text{m}$ ) that shows incipient alteration. NanoSIMS imaging of the section confirmed the C and N isotopic anomalies in both grains, although as in other FIB sections, the degree of  $^{15}\text{N}$  enrichment is less than the original value ( $\delta^{15}\text{N} = 700\text{--}735\text{‰}$  vs.  $1055\text{‰}$ ; Table 3). For C, however, both grains are somewhat more  $^{13}\text{C}$ -rich than the original measurement ( $\delta^{13}\text{C} = 125\text{--}130\text{‰}$  vs.  $100\text{‰}$ ).

*Area 5a-8:* This FIB section was cut through two parts of a large  $^{15}\text{N}$ -rich region (Fig. 11). The N-anomalous region consists of two distinct areas of compact organic particles that extend into the interior of the section (Fig. 12a). The surrounding material consists of abundant amorphous silicates and minor phyllosilicates, together with nanosulfides. A large Fe-(hydr)oxide grain is also present at depth. Further descriptions and images of this FIB

section are provided in Le Guillou and Brearley (2013). Isotope imaging shows that both areas are enriched in  $^{15}\text{N}$  (Table 3). However, in the original NanoSIMS imaging measurement, area 1 exhibited a significantly higher degree of  $^{15}\text{N}$  enrichment than area 2 (Fig. 11b), whereas the reverse is true in the FIB section (Fig. 12c). There are no morphological differences or other obvious distinctions between the carbonaceous matter in the two areas that might account for the difference. However, energy-filtered TEM (EFTEM) imaging does show the presence of N in area 2 (Fig. 13a), in contrast to other areas imaged, where N is below detection limits (Fig. 13b–d).

## 4. DISCUSSION

### 4.1. Nitrogen isotopic anomalies in QUE 99177 and MET 00426

The N isotopic compositions measured here are broadly consistent with those measured in residues of insoluble organic matter extracted from these meteorites. The average  $^{15}\text{N}$  enrichment of  $195\text{‰}$  measured in matrix areas from QUE 99177 (Table 1) is in good agreement with the bulk IOM value of  $190\text{‰}$  reported by Alexander et al. (2007). However, the matrix average of  $105\text{‰}$  for MET 00426 is

Table 3  
Isotopic compositions in MET 00426 FIB sections.

Sample	$^{14}\text{N}/^{15}\text{N}$	$\delta^{15}\text{N}$ (‰)	$^{12}\text{C}/^{13}\text{C}$	$\delta^{13}\text{C}$ (‰)
<i>Section 5b-6</i>				
5b-6c1 (original)			79.1 ± 1.0	138 ± 14
5b-6c1			82.5 ± 2.0	91 ± 26
C1			85.8 ± 2.6	48 ± 31
C2			89.0 ± 3.3	11 ± 37
C3			91.5 ± 1.1	−16 ± 12
<i>Section 5b-9</i>				
5b-9 hs1 (original)	121 ± 3	1242 ± 52	87.5 ± 1.2	28 ± 14
5b-9 hs1	181 ± 5	502 ± 38	88.2 ± 1.1	20 ± 13
C1	217 ± 5	251 ± 31	88.8 ± 1.8	14 ± 21
C2	215 ± 4	267 ± 24	85.8 ± 0.8	49 ± 10
C3	282 ± 7	−34 ± 25	87.1 ± 1.1	34 ± 13
<i>Section 1a-11</i>				
1a-11 hs1 (original)	126 ± 3	1158 ± 57		
1a-11 hs1	144 ± 6	887 ± 75	88.0 ± 1.6	22 ± 18
<i>Section 1a-15</i>				
C 1	258 ± 23	53 ± 95	96.0 ± 3.8	−62 ± 37
C 2	246 ± 14	104 ± 60	86.5 ± 1.0	41 ± 12
<i>Section 1a-17</i>				
1a-17 hs1 (original)	139 ± 5	956 ± 70	87.0 ± 2.0	34 ± 24
1a-17 hs1	161 ± 4	690 ± 41	82.6 ± 1.6	90 ± 21
R 1	195 ± 5	393 ± 35	87.4 ± 1.3	29 ± 15
R 2	244 ± 5	115 ± 22	88.3 ± 1.0	20 ± 12
R 3	234 ± 3	164 ± 16	87.3 ± 0.4	31 ± 5
<i>Section 6d-2</i>				
6d-2 hs1 (original)	132 ± 2	1056 ± 34	81.9 ± 0.8	99 ± 11
6d-2 hs1 1	160 ± 2	703 ± 22	79.9 ± 0.5	126 ± 8
6d-2 hs1 2	157 ± 2	735 ± 24	79.5 ± 0.6	132 ± 9
C 3	296 ± 9	−81 ± 27	88.2 ± 1.3	21 ± 15
<i>Section 5a-8</i>				
Area 1	222 ± 3	226 ± 18	85.3 ± 0.3	55 ± 4
Area 2	176 ± 2	550 ± 20	88.2 ± 0.2	20 ± 2

somewhat lower than the bulk IOM value (175‰; Alexander et al., 2007). To some extent the difference reflects the inclusion of one matrix area (area 1) in our study, which shows little overall enrichment in  $^{15}\text{N}$  (Table A2). However, an average of the MET 00426 matrix measured here, excluding this area, also falls somewhat short of the bulk IOM value ( $\delta^{15}\text{N} = 140\text{‰}$ ). Our in situ measurements include both the soluble and insoluble organic matter present in these meteorites. Isotopic measurements of soluble organic matter from CR chondrites indicates that they are also enriched in  $^{15}\text{N}$ , although to a lesser degree than insoluble organic matter (100–125‰; Pizzarello and Holmes, 2009). The discrepancy between the N isotopic composition of the matrix determined here and that determined by Alexander et al. (2007) for bulk IOM from MET 00426 is likely due to the fact that the organics (both soluble and insoluble) in these meteorites show both compositional and spatial heterogeneity; the areas measured in our study come from a single thin section, which may not be sufficient in all cases to statistically reproduce the more representative values obtained from bulk IOM. The hotspots in both meteorites show similar ranges in their N isotopic compositions (Table 1) and the

distributions are broadly similar to the N isotopic compositions observed for hotspots in IDPs (Fig. 1). However, the maximum  $^{15}\text{N}$  enrichments in the hotspots are higher than in IDPs and are similar to those reported for IOM from primitive meteorites (Busemann et al., 2006), although they do fall short of the enrichments observed in Isheyevo, the meteorite with the most  $^{15}\text{N}$ -rich compositions reported to date (Briani et al., 2009; Bonal et al., 2010).

For most of the FIB sections from MET 00426, we also measured the C and N isotopic compositions, allowing us to compare these analyses with the original identifying measurements. Except for localized hotspots, the C isotopic compositions in the FIB sections are normal, just as they are in the original measurements. Two of the grains we targeted for FIB-TEM analysis exhibited  $^{13}\text{C}$  enrichments. In the isotopically anomalous nanoglobule, 5b-6c1, the C isotopic composition measured in the FIB section is consistent, within  $2\sigma$  errors, with the one measured originally (Table 3). The hotspot from area 6d-2, actually consisted of two discrete grains (Fig. 11); both grains have  $^{13}\text{C}$  enrichments that are somewhat higher than the original value, although only at the  $3\sigma$  level (Table 3). In contrast, N isotopic compositions in the FIB sections are consistently less

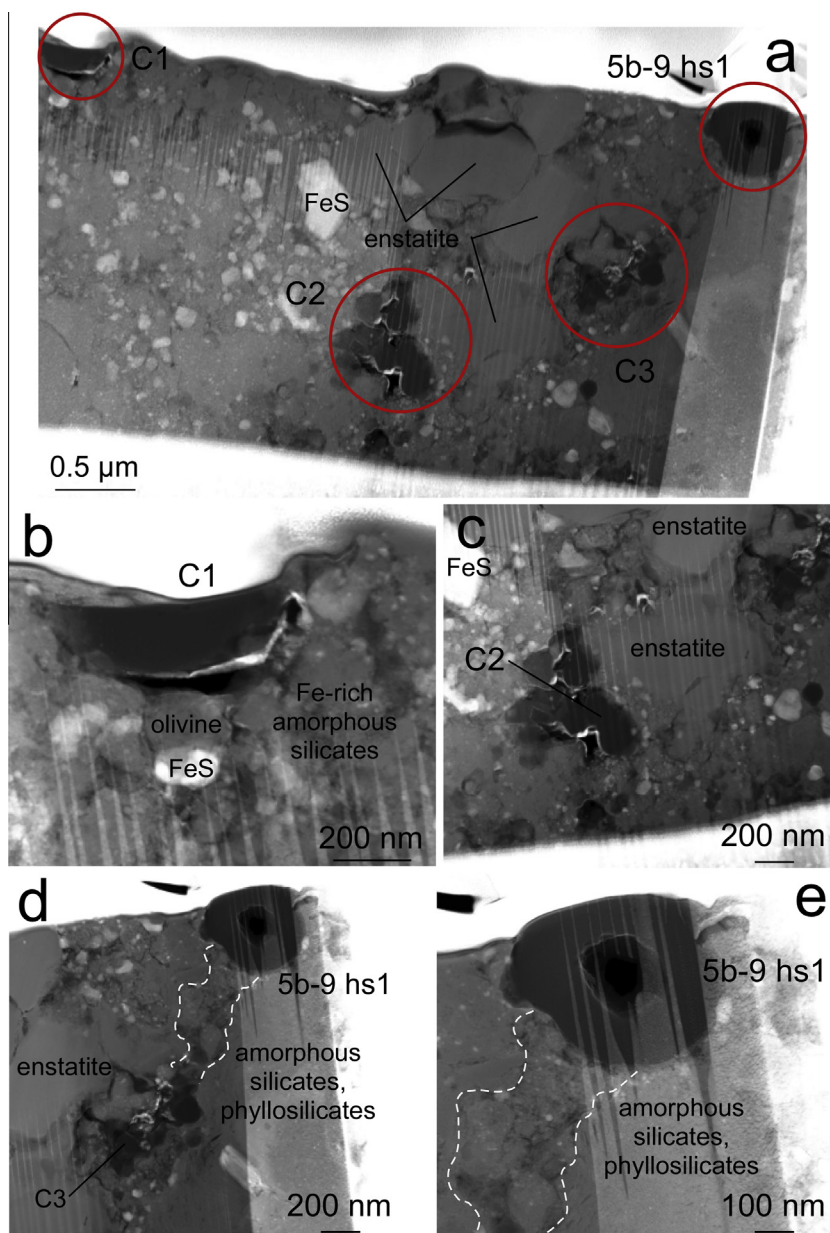


Fig. 6. MET 00426 matrix area 5b-9: (a) dark field STEM image of FIB section; (b) isotopically normal grain; (c) aggregate of C-rich grains and enstatite with alteration rim; (d) isotopically anomalous nanoglobule with normal aggregate of grains; (e) detailed view of nanoglobule showing vein of intermingled carbonaceous matter and nanophyllosilicates (dashed lines). Designations (5b-9 hs1, C1–C3) refer to NanoSIMS analyses presented in [Table 3](#).

$^{15}\text{N}$ -rich than the values obtained from the original NanoSIMS measurements. This is true not only for the average N isotopic compositions of the sections, but also for the hotspots targeted for analysis. Typically the change is on the order of 200–300‰, but in one instance, the isotopic anomaly measured in the FIB section is more than 700‰ lower than the original value (5b-9 hs1; [Table 3](#)). One possible explanation for this phenomenon is the loss of a labile  $^{15}\text{N}$ -rich carrier due to electron beam damage. Another, more likely, possibility is contamination with isotopically normal atmospheric N, resulting in dilution of the isotopic anomalies. This could result from the electron irradiation in

the TEM or FIB-SEM, which may have created defects in the molecular structure, allowing enhanced absorption of atmospheric N.

#### 4.2. Elemental compositions of C-rich matter in QUE 99177 and MET 00426

The Auger spectra determined for C-rich areas (both N-anomalous and isotopically normal) provide some information about the elemental make-up of these grains. The presence of S and the large range in S/C ratios in grains from QUE 99177 ([Table 2](#)) are both consistent with the

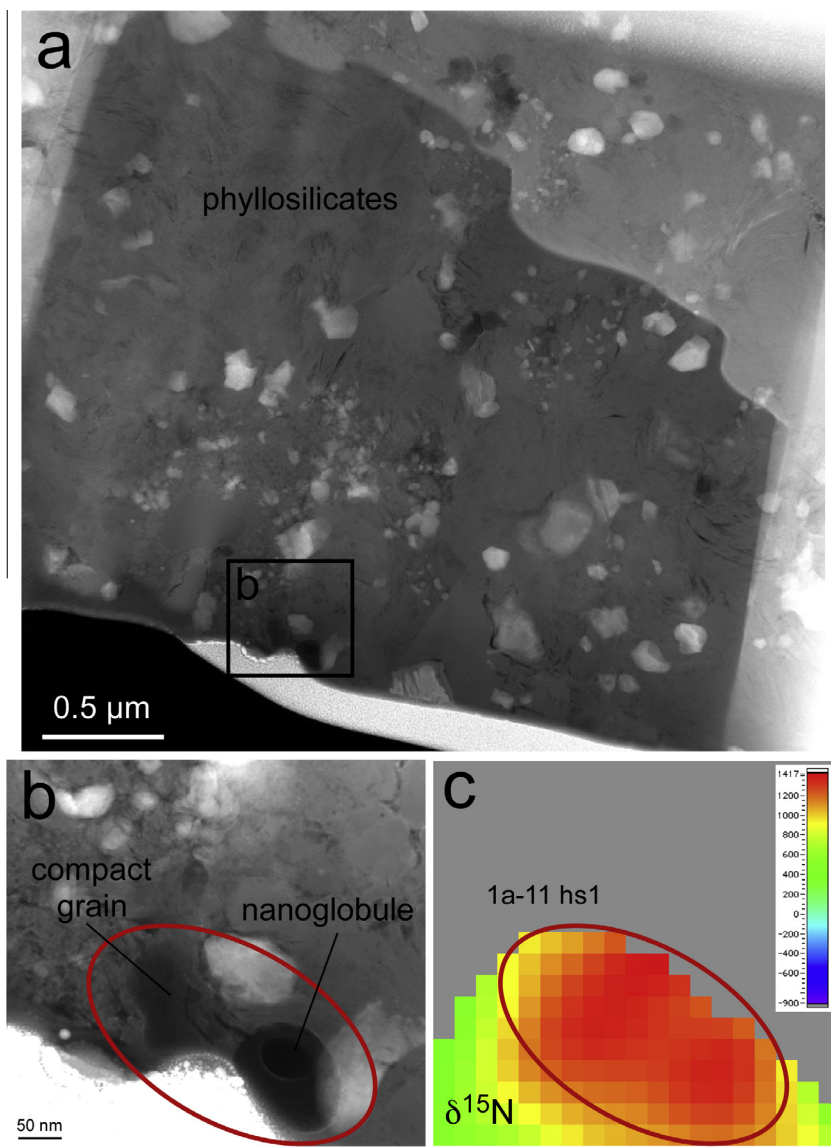


Fig. 7. MET 00426 matrix area 1a-11: (a) dark field STEM image of FIB section; (b) detail of the hotspot consisting of a nanoglobule with an attached compact carbonaceous grain; (c) NanoSIMS false color isotope ratio image of the area shown in (b). Designations (1a-11 hs1) refer to NanoSIMS analyses presented in Table 3.

primitive nature of the carbonaceous matter in this meteorite (Abreu and Brearley, 2010). These authors have also noted the presence of detectable N in the IOM from this meteorite, but we were able to observe N in only a few instances (Table 2). NanoSIMS measurements provide some complementary information.  $CN^-/C^-$  ratios show similar ranges in the two meteorites, both those determined for the hotspots as well as the average values calculated for each matrix area (Table 1). Applying earlier measurements of several kerogen standards (Floss et al., 2010), we can use the  $CN^-/C^-$  ratios to determine atomic N/C ratios for the carriers of the N isotopic anomalies. The N/C ratios calculated for the hotspots from both meteorites range from 0.0038 to 0.0224. This is consistent with those N/C ratios we were able to determine from Auger spectra taken of C-rich regions from QUE 99177 (Table 2), although the

latter tend to be at the high end of the range calculated from the NanoSIMS  $CN^-/C^-$  ratios. The difference can be attributed to the relatively high detection limits in the Auger Nanoprobe; N/C ratios could only be determined for areas with N contents of greater than about 1.5 at.%. The N/C ratios calculated here from the  $CN^-/C^-$  ratios are lower than those reported by Alexander et al. (2007) for bulk IOM from QUE 99177 (0.0365) and MET 00426 (0.0339). However, our in situ NanoSIMS measurements include not just the organic matter itself, but also other phases intimately intermingled with the carbonaceous material. The difference between our measurements and those of Alexander et al. (2007), thus, may be the result of matrix effects in the NanoSIMS analyses.

Fig. 2a shows that there is a general increase in the degree of  $^{15}N$  enrichment with higher  $CN^-/C^-$  ratios in

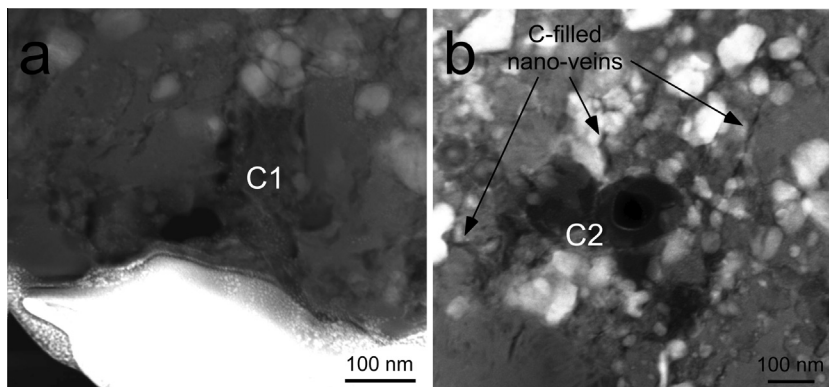


Fig. 8. Dark field STEM images of FIB section 1a-15 from MET 00426: (a) aggregate of isotopically normal carbonaceous matter; (b) two adjacent isotopically normal nanoglobules present in the interior of the section, surrounded by amorphous silicates, sulfides and nano-veins filled with C. Designations (C1–C2) refer to NanoSIMS analyses presented in Table 3.

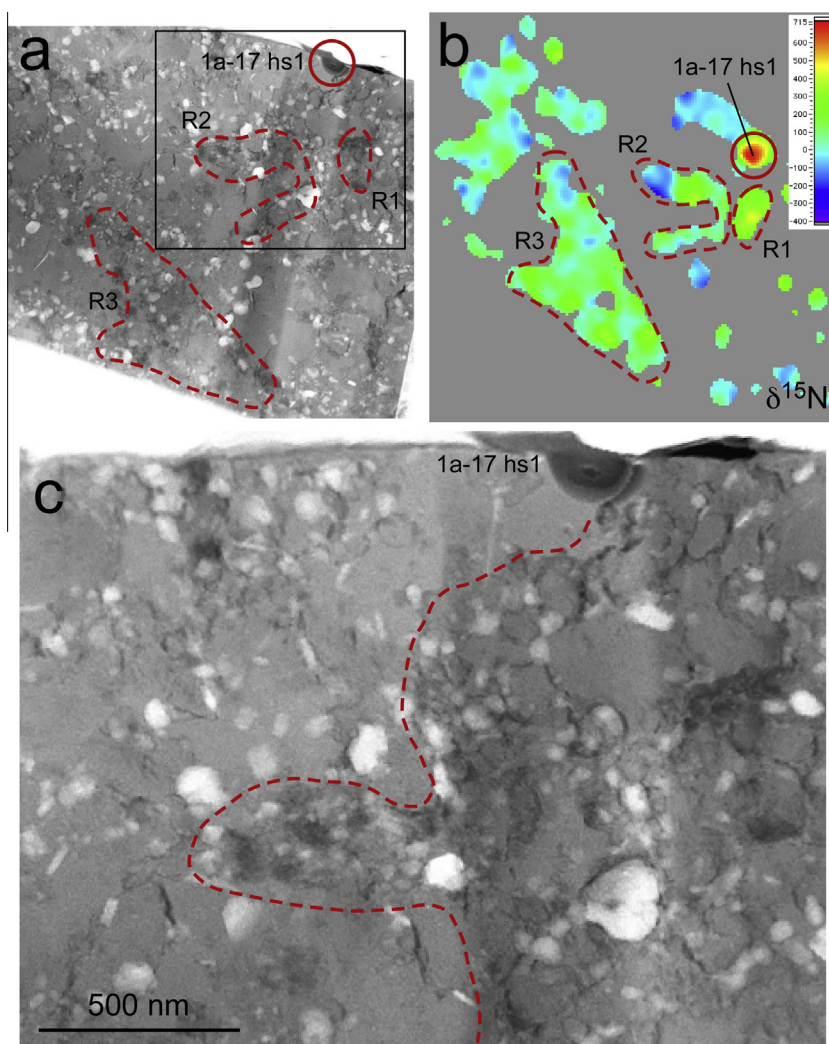


Fig. 9. MET 00426 matrix area 1a-17: (a) dark field STEM image of FIB section 1a-17; (b) NanoSIMS false color isotope ratio image of FIB section 1a-17; (c) close-up dark field STEM image of the area outlined in (a). The dashed lines in (a) and (b) show areas with enrichments in  $^{15}\text{N}$  and correspond to more altered regions containing phyllosilicates and fine-grained carbonaceous matter. Designations (1a-17 hs1, R1–R3) refer to NanoSIMS analyses presented in Table 3. The dashed line in (c) separates a more altered area with abundant organic matter, porosity and  $^{15}\text{N}$ -enriched regions (right) from a less altered area with fewer organics, less porosity and larger amorphous silicate domains (left).

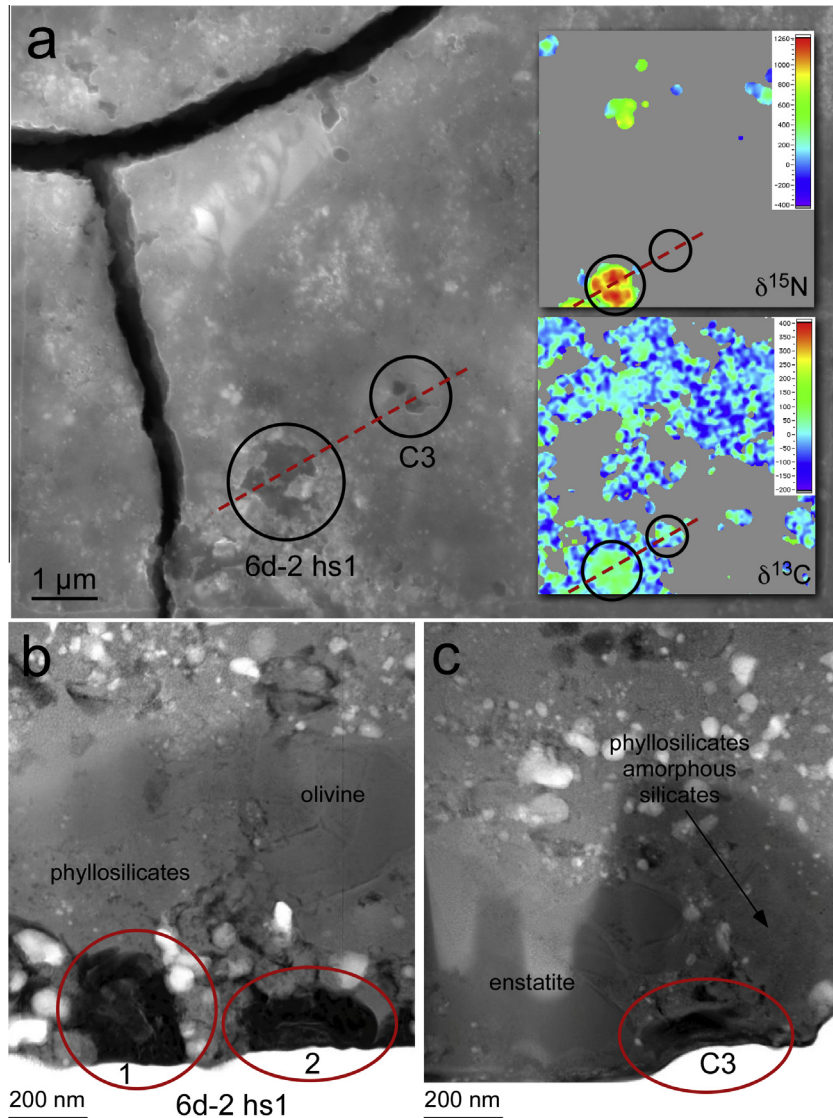


Fig. 10. MET 00426 matrix area 6d-2: (a) secondary electron image of area 6d-2, showing the line of the FIB cut through the C and N-anomalous hotspot 6d-2 hs1 and an isotopically normal grain, labeled C3; the inset shows NanoSIMS false color isotope ratio images of the area; (b) dark field STEM image of the FIB section through hotspot 6d-2 hs1, which consists of two separate grains associated with olivine, sulfides and phyllosilicates; (c) dark field STEM image of the FIB section through the isotopically normal grain C3, surrounded by enstatite, and mixed phyllosilicates and amorphous silicates. Designations (6d-2 hs1, C3) refer to NanoSIMS analyses presented in Table 3. Field of view for the NanoSIMS images is 10  $\mu\text{m}$ .

the main group of matrix areas. This trend likely reflects higher proportions of isotopically anomalous carbonaceous matter in those areas. As noted previously, some of the data fall off of this main trend, suggesting that some matrix areas are dominated by compositionally distinct organic matter. Evidence for this is also observed in the data for the hotspots. In contrast to the trend observed in the matrix areas, the N isotopic compositions of the hotspots are not correlated with their  $\text{CN}^-/\text{C}^-$  ratios (Fig. 2b). Instead, for any given  $\text{CN}^-/\text{C}^-$  ratio, the hotspots show a wide range of  $\delta^{15}\text{N}$  values, consistent with previous suggestions that a variety of distinct carbonaceous components carry the N isotopic anomalies observed in extraterrestrial materials (e.g., Cody et al., 2008; Busemann et al., 2009; Aléon, 2010). In previous work on IDPs we have observed an

inverse relationship between N isotopic compositions and elemental abundance (Floss et al., 2006, 2010); as N concentrations increased in the IDPs the range in the magnitude of the anomalies decreased, suggesting that contamination with isotopically normal N was diluting the isotopic anomalies. The source of this contamination (pre-terrestrial or during atmospheric entry heating) was not identified, but the fact that a similar trend is not observed in the data from this study argues in favor of the latter (e.g., Füri et al., 2013).

#### 4.3. Morphologies and petrographic associations

The FIB sections we investigated included a variety of C-rich grains from the matrix of MET 00426, with

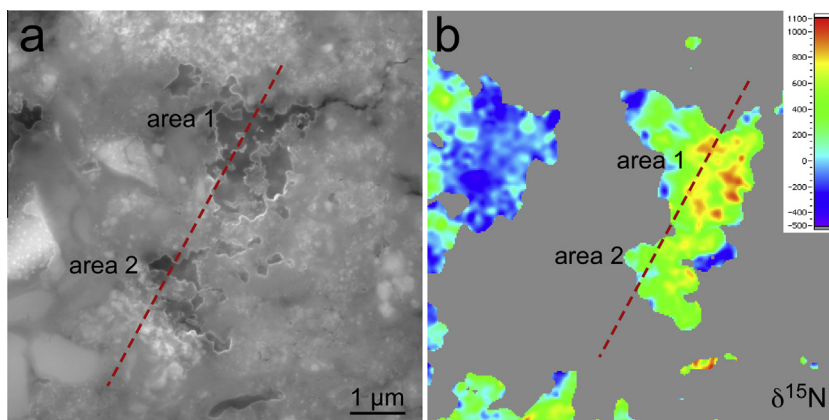


Fig. 11. Secondary electron image (a) and NanoSIMS false color isotope ratio image (b) of MET 00426 matrix area 5a-8, showing the line of the FIB cut through a large N-anomalous area. Field of view for the NanoSIMS image is 10  $\mu\text{m}$ . The FIB section for this matrix area is shown in Fig. 12.

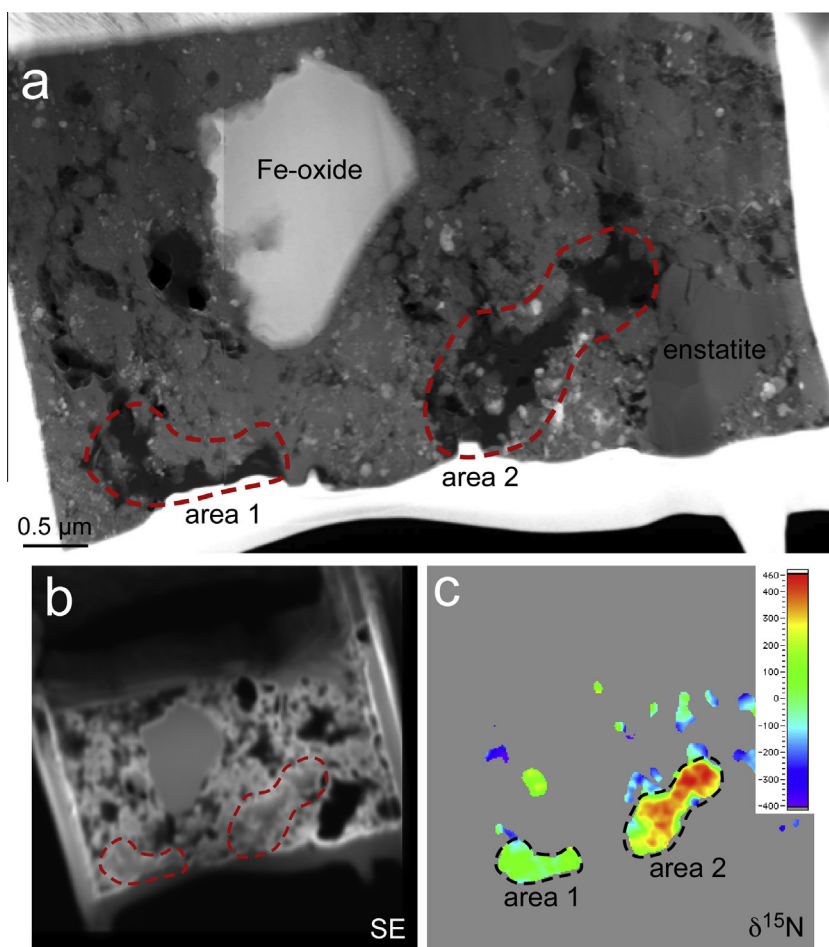


Fig. 12. MET 00426 matrix area 5a-8: (a) dark field STEM image of the FIB section showing N-anomalous areas 1 and 2; (b) secondary electron and (c) NanoSIMS isotope ratio image of the section. Designations (area 1, area 2) refer to NanoSIMS analyses presented in Table 3. Field of view for the NanoSIMS images is 10  $\mu\text{m}$ .

N-anomalous grains, C-anomalous grains and grains that are isotopically normal all represented. Our observations indicate that all grains examined are structurally similar

in that they consist of highly disordered carbonaceous matter, e.g., no graphitized organic matter was found. However, the morphologies of the grains showed large

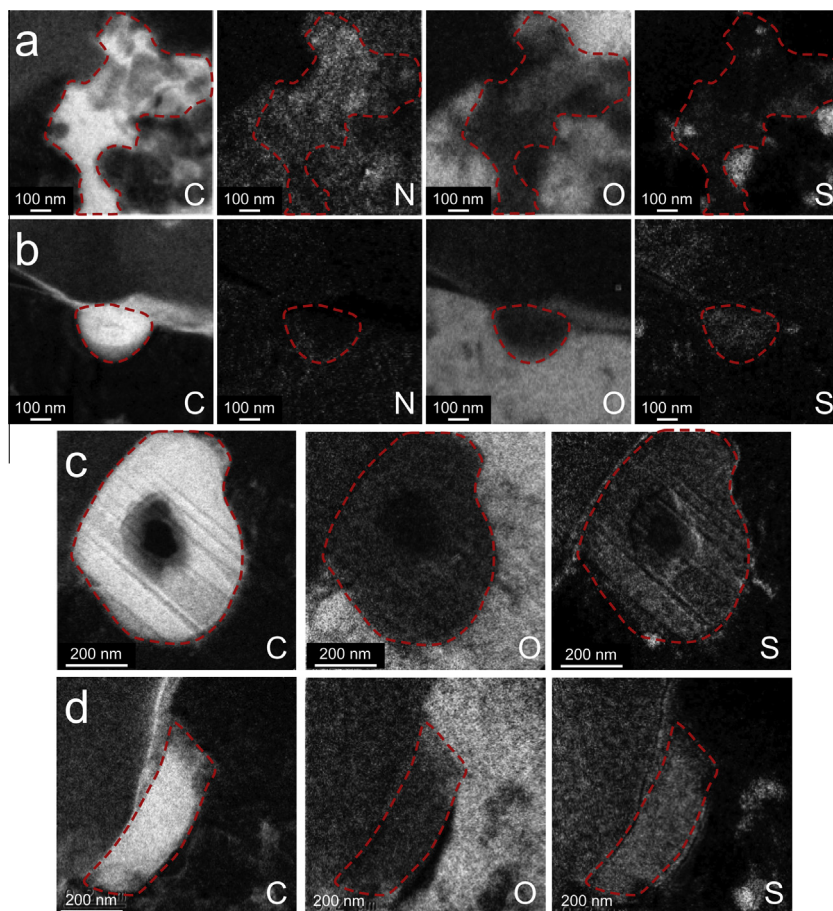


Fig. 13. Energy-filtered TEM elemental maps of carbonaceous grains from MET 00426: (a)  $^{15}\text{N}$ -rich area 2 from section 5a-8; (b) N-anomalous nanoglobule from section 1a-17; (c) N-anomalous nanoglobule from section 5b-9; (d) isotopically normal C-rich grain from section 5b-9.

variations. Some grains are hollow nanoglobules, while others have compact rounded or blocky morphologies. Aggregates of grains are also present, and can consist of nanoglobules or blocky grains, as well as less defined shapes. Perhaps most notable in this regard is the region associated with hotspot 1a-11, which encompasses a hollow nanoglobule and an adjacent irregular grain (Fig. 7). Although the two grains appear quite distinct, the N isotopic anomaly is clearly associated with both of them (Fig. 7b and c). In some instances,  $^{15}\text{N}$ -rich hotspots continue as veins or pockets in the interiors of the sections (e.g., Fig. 12). Isotopically normal veins of carbonaceous matter are also present and may be associated with either  $^{15}\text{N}$ -rich grains and aggregates of grains, or isotopically normal grains (e.g., section 5b-9, Fig. 6). The different morphologies observed in these sections do not show any obvious correlation with isotopic composition. For the most part there are also no clear elemental distinctions between anomalous and isotopically normal grains. For example, EFTEM images and EDS analyses show the presence of S in all grains, and the absence of detectable N in most. An exception is area 2 from FIB section 5a-8 (Fig. 12). This C-rich region is the only one measured in this study to show the presence of detectable N by EFTEM imaging (Fig. 13).

Area 2 is enriched in  $^{15}\text{N}$  (Table 3), but otherwise shows no particular distinguishing characteristics (e.g., highest  $^{15}\text{N}$  enrichment, unusual morphology). Finally, there is also no obvious correlation of isotopically anomalous grains with the type of matrix environment in which they occur. Anomalous grains are found surrounded by both crystalline and amorphous silicates, as well as hydrated and anhydrous phases, and the same is true for isotopically normal grains. As discussed in more detail below, these observations are consistent with the formation of these grains through multiple pathways, and with suggestions that their isotopic signatures may be inherited from simpler precursor molecules.

#### 4.4. Effects of aqueous alteration

Most CR chondrites have experienced mild aqueous alteration (e.g., Krot et al., 2002). QUE 99177 and MET 00426 are exceptional in that they have been significantly less affected than most of the CRs, and have been classified as CR3 chondrites (Abreu and Brearley, 2010). Nevertheless, evidence for the presence of water and preliminary stages of alteration exists in the matrices of these meteorites (Bonal et al., 2013; Le Guillou and Brearley, 2013), and this

is observed in our study as well. Phyllosilicates, mainly consisting of very small (as little as a few nanometers) crystalline domains, and hydrated amorphous silicates form the groundmass of the matrix and surround many of the carbonaceous areas. In some instances, alteration rims are present around crystalline silicates (e.g., Fig. 6c). Veins and pockets of organic matter are also common in the sections studied here. These can consist of relatively large (micron-sized) compact aggregates or masses of carbonaceous matter, such as those observed in section 5a-8 (Fig. 12), or of fine grained (nanometer-scale) carbonaceous particles finely intermingled with nanophyllosilicates as seen in section 5b-9 (Fig. 6d and e). Thin carbon-bearing cracks or fractures are also found in the sections and are sometimes connected to individual particles or aggregates of organic matter (e.g. Fig. 5). Le Guillou et al. (in press) have argued that such veins and pockets are suggestive of fluid-driven redistribution of organic matter that likely accreted first as individual grains.  $^{15}\text{N}$ -rich soluble molecules (e.g., carboxylic acids, amino acids; Pizzarello and Holmes, 2009) present in the accreted organic constituents are the best candidates for this redistribution, as well as for potential interaction with the fluid.

Aqueous alteration is particularly evident in several sections from matrix area 1. Section 1a-11 (Fig. 7) is the most altered one in our study, with large phyllosilicate domains present throughout the section. Sections 1a-15 (Fig. 8) and 1a-17 (Fig. 9) are less recrystallized and contain regions with abundant amorphous silicates, as well as more extensively altered areas dominated by hydrated amorphous silicates, nanophyllosilicates and nanosulfides intricately mixed with small cracks and pockets of carbonaceous matter (Fig. 9c). NanoSIMS imaging of section 1a-17 shows that the more altered matrix areas are modestly enriched in  $^{15}\text{N}$ . In contrast to the highly localized hotspots typically observed, these  $^{15}\text{N}$  enrichments are more diffuse and spread out over larger areas (Fig. 9b). If the organic components in these altered regions formed through the action of fluid, as suggested by Le Guillou et al. (in press), the associated  $^{15}\text{N}$  enrichments, may have been redistributed from their original hosts to the surrounding matrix through the fluid, possibly as soluble species. This would be consistent with laboratory alteration experiments, which indicate that  $^{15}\text{N}$ -rich labile macromolecular organic matter in carbonaceous chondrites is easily removed through aqueous processing (Sephton et al., 2003). Alternatively, the carbonaceous material in these diffuse  $^{15}\text{N}$ -enriched regions may simply have accreted as more fine-grained components, e.g., as individual aggregates or as carbonaceous mantles on other constituents of the matrix. In both cases, mixing and dilution with isotopically normal neighboring material would lead to larger diffuse regions enriched in  $^{15}\text{N}$ , but to a lower degree than the more concentrated and localized hotspots that are also observed.

As noted earlier, matrix area 1 appears to be less  $^{15}\text{N}$ -rich than other matrix areas in MET 00426, with an average  $^{15}\text{N}$ -enrichment of  $\sim 50\%$  compared to  $\sim 140\%$  for the other matrix areas analyzed. The two other sections we examined from matrix area 1, 1a-11 and 1a-15, do not show regions with diffuse  $^{15}\text{N}$  enrichments like those seen

in section 1a-17, although they appear to have experienced similar degrees of aqueous alteration. Instead, N isotopic compositions are normal in both sections, with the exception of the  $^{15}\text{N}$ -rich hotspot in 1a-11. However, both sections also contain significantly less carbonaceous matter than section 1a-17. This indicates that heterogeneous accretion of organic material in different regions of the matrix plays an important role in establishing the N isotopic compositions of these areas.

Ultimately, our data do not provide definitive constraints on whether or not carbonaceous matter in MET 00426 has been redistributed via fluid action, as suggested by Le Guillou et al. (in press). However, we note that bulk  $^{15}\text{N}$  enrichments in the IOM of more altered CR2 and CR1 chondrites do not differ substantially from those in QUE 99177 and MET 00426 (Alexander et al., 2007). This suggests that, if fluid action did indeed redistribute or alter organic matter in this meteorite group, it did so in a closed system, without significantly modifying the chemistry of the insoluble fraction of the OM as measured by Alexander et al. (2007).

#### 4.5. Formation of N-anomalous matter in solar system materials

The possible origins of the N isotopic anomalies observed in the carbonaceous matter of primitive meteorites and IDPs have been extensively reviewed and generally advocate either an interstellar or cold molecular cloud origin via low-temperature ion–molecule reactions (e.g., Terzieva and Herbst, 2000; Rodgers and Charnley, 2008; Aléon, 2010), or a solar system origin via photochemical self-shielding (e.g., Clayton, 2002; Lyons et al., 2009). The experimental reproduction, via VUV photolysis, of enrichments in  $^{15}\text{N}$  similar to those observed in meteoritic IOM (Chakraborty et al., 2013) may indeed provide a viable solar system mechanism for fractionating N. However, the recent observation of  $^{15}\text{N}$  enhancements in two dense prestellar cores (Hily-Blant et al., 2013) and variations in the N isotopic ratio across the Galaxy (Adande and Ziurys, 2012) have also strengthened arguments for an interstellar origin.

Rodgers and Charnley (2008), focusing on the formation of ammonia ( $\text{NH}_3$ ), showed that  $^{15}\text{N}$  enrichments of more than 3000‰ could be produced in dense molecular clouds at very low temperatures. More recently, Wirstrom et al. (2012) recognized that isotopic fractionation of both N and H in ion–molecule reactions is highly dependent on the spin-state of  $\text{H}_2$ , due to a large difference in the zero-point energies between the para (antiparallel spins) and ortho (aligned nuclear spins) forms. Modeling ion–molecule reactions with this parameter taken into account, they concluded that the functional groups carrying N isotopic anomalies, nitriles and amines, can exhibit a wide range of fractionations, with the largest  $^{15}\text{N}$  enrichments carried by nitriles. More significantly, this model can also account for the  $^{15}\text{N}$ -depleted ‘coldspots’ that are also occasionally observed in QUE 99177 and MET 00426 (e.g., Fig. 1); low degrees of  $^{15}\text{N}$  enrichment and even depletions in  $^{15}\text{N}$  are expected to occur in ion–molecule reactions involving  $\text{H}_2$ ,  $\text{NH}_3$  and related molecules (Wirstrom et al., 2012).

The large range of isotopic fractionations predicted from this model is consistent with the range of isotopic anomalies observed in meteoritic OM, and provides a mechanism for producing simple molecules with variable isotopic compositions from which the macromolecular organic matter hosting these isotopic anomalies can be derived.

Laboratory experiments under temperature and pressure conditions similar to those expected in cold molecular clouds have shown that UV photolysis can easily convert icy interstellar analogs to complex organic compounds (Bernstein et al., 2002, 2003). Such a formation process would take place in environments with different proportions of gas, dust and ice-mantled grains, and could produce organic matter with a range of morphologies, as observed for the carbonaceous grains in our work. Ciesla and Sandford (2012) questioned, however, to what extent this matter could be preserved during the formation of the solar system, and suggested that the outer regions of the solar system provide a similar environment, allowing for the formation of complex organic compounds during evolution of the protoplanetary disk. Modeling this process, they showed that irradiation and warming of ices to synthesize fresh organic matter is a natural consequence of the dynamical evolution of the solar system. The ion–molecule reactions responsible for the isotopic fractionations could also take place in the cold outer regions of the protoplanetary disk, allowing for a solar system origin for N isotopic fractionations that is indistinguishable from an interstellar one.

Formation of both isotopically anomalous and normal carbonaceous grains, such as those in our study, thus, likely took place in a number of different settings and under different conditions, with the variable morphologies and isotopic compositions observed resulting from the specific environment in which each grain formed. Moreover, secondary alteration appears to be responsible for some of the petrographic features observed (e.g., the presence of veins and cracks filled with organic matter; Le Guillou and Brearley, 2013). Ultimately it may not be possible in

most cases to distinguish an interstellar origin from an origin in the outer solar nebula for the carbonaceous matter found in these meteorites. The direct association of presolar grains with such organic matter may be one exception (e.g., Messenger and Keller, 2005), but such associations are rare.

## 5. CONCLUSIONS

As in other CR chondrites, the organic matter in the primitive CR3s QUE 99177 and MET 00426 has N isotopic compositions that are characterized by large enrichments in  $^{15}\text{N}$  compared to solar. These enrichments are present in as localized hotspots and as larger diffuse regions with more modest enrichments in  $^{15}\text{N}$ . Occasionally depletions in  $^{15}\text{N}$  are also observed. FIB-TEM analysis shows that all of the organic matter, whether isotopically anomalous or isotopically normal, is highly disordered and exhibits a variety of morphologies. Isotopic compositions are not correlated with morphology, petrographic association or elemental composition. Large diffuse regions with modest  $^{15}\text{N}$  enrichments may be the result of fluid action that redistributed organic matter (and the associated  $^{15}\text{N}$  enrichments) in veins and cracks along grain boundaries. The organic matter found in these meteorites probably formed in a variety of environments (e.g., molecular clouds or the outer regions of the protosolar nebula) via UV photolysis of simpler precursor ices with variable isotopic compositions.

## ACKNOWLEDGEMENTS

This work was supported by NASA's Cosmochemistry Program through grants NNX10AI64G (PI: C. Floss), NNG06GG37G and NNX11AK51G (PI: A. Brearley). We gratefully acknowledge the careful and constructive reviews by three anonymous reviewers, which significantly improved this paper. Electron beam analysis at the University of New Mexico was carried out in the Electron Microbeam Analysis Facility, Department of Earth and Planetary Sciences. The facility is supported by funds from the State of New Mexico, the National Science Foundation and NASA.

## APPENDIX

Table A1  
Nitrogen and C isotopic compositions of matrix and hotspots in QUE 99177.

Area	$^{14}\text{N}/^{15}\text{N}$	$\delta^{15}\text{N}$ (‰)	$^{12}\text{C}/^{13}\text{C}$	$\delta^{13}\text{C}$ (‰)	$\text{CN}^-/\text{C}^-$
2a-1	182 ± 2	492 ± 17	91.3 ± 0.7	−15 ± 8	1.37
hs1	107 ± 2	1543 ± 49	88.3 ± 1.2	19 ± 14	0.94
hs2	123 ± 2	1216 ± 39	91.3 ± 1.3	−14 ± 14	1.19
2a-2	227 ± 3	199 ± 14	90.6 ± 0.7	−7 ± 8	1.42
hs1	123 ± 4	1216 ± 70	94.6 ± 2.8	−49 ± 28	1.86
2a-3	225 ± 3	210 ± 15	90.3 ± 0.7	−3 ± 8	1.02
hs1	123 ± 3	1209 ± 62	97.8 ± 2.1	−80 ± 20	1.19
2a-4	209 ± 2	300 ± 15	91.3 ± 0.7	−14 ± 7	0.89
hs1	95 ± 1	1867 ± 40	97.8 ± 1.0	−80 ± 9	1.05
2b-1	238 ± 3	142 ± 13	90.3 ± 0.7	−3 ± 8	0.99
hs1	139 ± 6	955 ± 81	91.8 ± 2.3	−19 ± 25	0.94

(continued on next page)

Table A1 (continued)

Area	$^{14}\text{N}/^{15}\text{N}$	$\delta^{15}\text{N}$ (‰)	$^{12}\text{C}/^{13}\text{C}$	$\delta^{13}\text{C}$ (‰)	$\text{CN}^-/\text{C}^-$
2b-2	236 ± 3	153 ± 13	91.4 ± 0.7	-16 ± 7	0.94
hs1	106 ± 5	1565 ± 125	101.3 ± 3.6	-112 ± 31	0.91
hs2	126 ± 6	1154 ± 98	99.2 ± 2.6	-92 ± 24	0.77
2b-3	227 ± 3	199 ± 13	92.7 ± 0.7	-29 ± 7	1.17
hs1	115 ± 4	1372 ± 76	99.9 ± 2.0	-99 ± 19	0.79
hs2	122 ± 4	1229 ± 66	95.8 ± 1.8	-60 ± 18	0.85
2b-4	230 ± 3	182 ± 14	92.0 ± 0.7	-22 ± 7	0.86
hs1	122 ± 4	1224 ± 75	93.1 ± 1.9	-33 ± 20	0.74
2b-5	240 ± 3	131 ± 13	91.2 ± 0.7	-13 ± 7	0.86
2b-6	233 ± 3	169 ± 14	90.3 ± 0.7	-4 ± 8	0.83
hs1	140 ± 6	944 ± 85	89.8 ± 2.3	3 ± 26	0.80
2c-1	236 ± 3	151 ± 14	90.8 ± 0.7	-8 ± 8	0.89
*hs1	293 ± 19	-72 ± 59	120.9 ± 3.9	-256 ± 24	0.96
2c-2	229 ± 3	190 ± 15	90.6 ± 0.7	-6 ± 8	0.75
hs1	144 ± 3	892 ± 45	94.6 ± 1.2	-49 ± 12	0.54
2c-3	236 ± 3	151 ± 14	n.d.	n.d.	
2c-4	229 ± 3	189 ± 14	n.d.	n.d.	
hs1	120 ± 6	1258 ± 104	n.d.	n.d.	
2c-5	222 ± 3	224 ± 14	n.d.	n.d.	
hs1	125 ± 4	1170 ± 70	n.d.	n.d.	
2c-6	240 ± 3	134 ± 13	n.d.	n.d.	
5a-1	235 ± 3	156 ± 14	89.6 ± 0.7	5 ± 8	0.67
5a-2	236 ± 3	151 ± 13	89.8 ± 0.7	2 ± 7	1.25
*hs1	114 ± 4	1380 ± 80	105.2 ± 2.3	-144 ± 19	1.25
5a-3	239 ± 3	140 ± 14	89.6 ± 0.7	5 ± 8	0.76
hs1	114 ± 11	1376 ± 233	93.5 ± 3.8	-38 ± 39	0.45
hs2	136 ± 4	1002 ± 62	89.7 ± 1.7	4 ± 19	1.14
hs3	146 ± 6	866 ± 72	86.4 ± 1.3	41 ± 16	0.52
*hs4	253 ± 9	76 ± 39	106.5 ± 2.4	-155 ± 19	1.95
5a-4	217 ± 2	251 ± 14	89.4 ± 0.7	7 ± 8	1.39
hs1	366 ± 16	-257 ± 32	93.7 ± 3.0	-40 ± 31	4.70
hs2	119 ± 3	1290 ± 56	87.3 ± 1.4	31 ± 17	1.34
5a-5	224 ± 3	216 ± 14	89.6 ± 0.7	5 ± 8	0.81
5a-6	208 ± 2	308 ± 15	89.9 ± 0.7	1 ± 7	1.50
hs1	147 ± 4	849 ± 47	89.8 ± 1.5	2 ± 17	1.72
5a-7	241 ± 3	131 ± 13	89.9 ± 0.7	1 ± 7	0.72
*hs1	127 ± 4	1144 ± 67	100.5 ± 1.0	-104 ± 9	0.34
hs2	148 ± 7	835 ± 84	87.1 ± 1.3	33 ± 16	0.34
5a-8	220 ± 2	236 ± 14	89.6 ± 0.7	5 ± 8	1.19
hs1	346 ± 15	-214 ± 33	98.0 ± 2.1	-82 ± 19	1.57
hs2	369 ± 22	-263 ± 45	93.9 ± 2.6	-42 ± 27	1.64
hs3	122 ± 5	1226 ± 86	94.8 ± 3.2	-51 ± 32	2.15
5a-9	245 ± 3	110 ± 13	89.8 ± 0.7	2 ± 7	0.69
hs1	142 ± 4	913 ± 57	93.1 ± 1.4	-33 ± 15	0.72
5a-10	229 ± 3	187 ± 14	90.1 ± 0.7	-1 ± 8	0.96
hs1	115 ± 7	1357 ± 137	97.2 ± 4.8	-74 ± 46	1.84
*hs2	331 ± 15	-177 ± 37	107.5 ± 3.2	162 ± 25	3.14
5b-1	255 ± 3	67 ± 14	89.4 ± 0.7	7 ± 8	0.36
hs1	156 ± 8	743 ± 88	84.9 ± 2.9	60 ± 36	1.79
5b-2	252 ± 3	78 ± 14	89.5 ± 0.7	6 ± 8	0.40
hs1	178 ± 7	531 ± 58	90.8 ± 1.3	-9 ± 15	0.56
5b-3	232 ± 3	171 ± 14	89.4 ± 0.7	7 ± 8	0.65
hs1	146 ± 4	869 ± 45	87.8 ± 1.5	25 ± 18	1.77
5b-4	225 ± 3	207 ± 14	90.1 ± 0.7	-1 ± 7	0.87
hs1	83 ± 7	2274 ± 259	99.2 ± 14.0	-92 ± 128	6.94
*hs2	316 ± 9	140 ± 24	80.5 ± 1.1	118 ± 15	2.17
5b-5	227 ± 3	199 ± 14	90.3 ± 0.7	-4 ± 8	1.93
hs1	109 ± 6	1491 ± 130	96.4 ± 5.3	-66 ± 51	3.14
hs2	118 ± 2	1296 ± 36	92.3 ± 1.2	-25 ± 13	2.46
5b-6	219 ± 3	244 ± 14	89.4 ± 0.7	7 ± 8	0.85
hs1	144 ± 2	885 ± 30	86.0 ± 0.8	47 ± 10	0.96

(continued on next page)

Table A1 (continued)

Area	$^{14}\text{N}/^{15}\text{N}$	$\delta^{15}\text{N}$ (‰)	$^{12}\text{C}/^{13}\text{C}$	$\delta^{13}\text{C}$ (‰)	$\text{CN}^-/\text{C}^-$
*hs2	157 ± 11	734 ± 119	108.4 ± 2.6	−170 ± 19	0.47
5b-7	215 ± 2	266 ± 15	89.9 ± 0.7	1 ± 7	0.74
hs1	112 ± 4	1421 ± 82	88.7 ± 2.1	15 ± 23	1.16
5b-8	264 ± 3	29 ± 12	89.9 ± 0.7	1 ± 7	0.65
hs1	368 ± 9	−261 ± 17	95.9 ± 1.0	−61 ± 10	0.94
hs2	120 ± 7	1265 ± 136	92.0 ± 4.1	−22 ± 44	1.39
5b-9	247 ± 3	101 ± 13	89.9 ± 0.7	1 ± 7	0.67
5b-10	249 ± 3	93 ± 13	89.9 ± 0.7	1 ± 8	0.72
5c-1	229 ± 3	186 ± 14	89.7 ± 0.7	4 ± 8	1.37
hs1	151 ± 4	797 ± 45	81.3 ± 1.9	107 ± 25	3.67
hs2	163 ± 3	665 ± 27	84.1 ± 1.2	70 ± 15	3.67
5c-2	221 ± 3	229 ± 14	89.8 ± 0.7	2 ± 8	1.03
hs1	161 ± 2	686 ± 23	93.5 ± 0.8	−38 ± 9	2.04
5c-3	233 ± 3	166 ± 13	89.8 ± 0.7	2 ± 7	1.23
hs1	136 ± 4	997 ± 56	89.4 ± 2.1	7 ± 24	2.64
hs2	173 ± 2	572 ± 21	85.0 ± 0.9	59 ± 11	4.44
5c-4	234 ± 3	163 ± 14	89.6 ± 0.7	5 ± 8	0.92
hs1	421 ± 23	−354 ± 36	99.4 ± 2.3	−94 ± 21	1.30
hs2	97 ± 10	1817 ± 305	99.4 ± 6.3	−94 ± 57	0.65
hs3	150 ± 3	808 ± 37	86.3 ± 0.9	43 ± 10	0.60
5c-5	206 ± 2	321 ± 15	89.3 ± 0.7	8 ± 8	1.30
hs1	109 ± 2	1502 ± 54	89.4 ± 1.3	7 ± 15	1.28
hs2	104 ± 5	1609 ± 129	90.2 ± 3.5	−3 ± 38	1.52
hs3	108 ± 8	1528 ± 185	93.2 ± 2.9	−35 ± 30	0.45
5c-6	189 ± 2	437 ± 16	90.6 ± 0.7	−7 ± 7	1.23
*hs1	118 ± 3	1297 ± 61	108.4 ± 2.6	−170 ± 19	2.04
*hs2	122 ± 4	1234 ± 72	109.0 ± 2.6	−174 ± 19	1.39
5c-7	206 ± 2	321 ± 15	90.1 ± 0.7	−1 ± 7	1.14
hs1	96 ± 4	1842 ± 131	95.6 ± 2.0	−58 ± 19	0.43
5c-8	221 ± 3	230 ± 14	89.8 ± 0.7	3 ± 7	0.78
hs1	97 ± 10	1796 ± 279	101.3 ± 4.3	−112 ± 38	0.38
5c-9	210 ± 2	296 ± 15	89.7 ± 0.7	4 ± 8	1.25
hs1	110 ± 5	1474 ± 110	89.3 ± 3.6	8 ± 40	2.22
hs2	124 ± 4	1193 ± 71	94.3 ± 1.8	−46 ± 18	0.92
5c-10	214 ± 2	271 ± 15	90.0 ± 0.7	−1 ± 7	0.72
hs1	141 ± 2	928 ± 30	95.4 ± 0.9	−56 ± 9	0.87
5c-11	237 ± 3	150 ± 14	89.6 ± 0.7	5 ± 8	0.60
hs1	136 ± 8	999 ± 111	92.1 ± 3.3	−23 ± 35	1.21
5c-12	247 ± 3	100 ± 13	89.8 ± 0.7	3 ± 7	0.83
5c-13	253 ± 3	74 ± 12	89.5 ± 0.7	6 ± 8	1.05
hs1	142 ± 5	912 ± 71	89.0 ± 2.1	12 ± 23	1.34
5c-14	181 ± 2	503 ± 18	89.3 ± 0.7	8 ± 8	1.01
hs1	91 ± 4	2002 ± 142	94.0 ± 4.4	−43 ± 45	1.93
hs2	101 ± 4	1685 ± 93	96.8 ± 2.7	−71 ± 26	1.52
5c-15	222 ± 3	223 ± 15	88.8 ± 0.7	14 ± 8	0.63
hs1	97 ± 2	1793 ± 59	94.5 ± 1.4	−48 ± 15	1.19
5c-16	264 ± 3	29 ± 12	89.6 ± 0.7	5 ± 8	1.01
hs1	152 ± 7	794 ± 83	90.3 ± 2.7	−4 ± 30	1.50
5c-17	228 ± 3	194 ± 14	89.6 ± 0.7	5 ± 8	0.99
hs1	113 ± 3	1399 ± 56	93.0 ± 1.4	−32 ± 15	1.32
5c-18	241 ± 3	127 ± 13	89.6 ± 0.7	5 ± 8	0.76
hs1	123 ± 7	1211 ± 119	89.5 ± 3.4	6 ± 38	1.25
hs2	125 ± 7	1170 ± 121	97.0 ± 4.6	−72 ± 44	1.75
5c-19	225 ± 3	208 ± 14	89.3 ± 0.7	8 ± 8	0.83
hs1	79 ± 4	2460 ± 180	97.6 ± 4.7	−78 ± 45	1.64
hs2	109 ± 5	1491 ± 114	91.3 ± 2.9	−14 ± 31	1.12
hs3	98 ± 5	1788 ± 136	96.8 ± 3.5	−71 ± 33	1.23
5c-20	223 ± 3	221 ± 14	89.8 ± 0.7	2 ± 7	0.92
hs1	117 ± 2	1323 ± 48	89.3 ± 1.4	8 ± 16	2.02
5c-21	230 ± 3	184 ± 14	89.6 ± 0.7	5 ± 8	0.85
5c-22	243 ± 3	119 ± 13	89.4 ± 0.7	7 ± 8	0.78

(continued on next page)

Table A1 (continued)

Area	$^{14}\text{N}/^{15}\text{N}$	$\delta^{15}\text{N}$ (‰)	$^{12}\text{C}/^{13}\text{C}$	$\delta^{13}\text{C}$ (‰)	$\text{CN}^-/\text{C}^-$
hs1	125 ± 10	1176 ± 170	97.2 ± 4.2	-74 ± 40	0.81
5c-23	247 ± 3	101 ± 13	89.9 ± 0.7	1 ± 8	1.05
5t-2	217 ± 2	256 ± 14	89.6 ± 0.7	5 ± 8	1.21
hs1	343 ± 21	-207 ± 49	89.3 ± 2.1	8 ± 24	1.05
hs2	132 ± 6	1067 ± 93	94.0 ± 2.4	-43 ± 25	0.90
6a-1	246 ± 3	105 ± 13	89.5 ± 0.7	6 ± 8	0.99
hs1	126 ± 3	1162 ± 48	86.7 ± 1.6	38 ± 19	2.40
6b-1	238 ± 3	144 ± 13	90.3 ± 0.7	-4 ± 7	0.90
hs1	147 ± 5	853 ± 65	89.8 ± 1.6	3 ± 18	0.85
6b-2	235 ± 3	157 ± 13	89.8 ± 0.7	2 ± 7	1.03
hs1	133 ± 2	1048 ± 30	86.7 ± 1.0	38 ± 12	2.62
6b-3	212 ± 2	283 ± 15	90.0 ± 0.7	-1 ± 7	1.19
hs1	104 ± 3	1616 ± 65	97.3 ± 2.5	-75 ± 24	0.49
hs2	89 ± 2	2046 ± 61	94.3 ± 1.7	-46 ± 17	1.93
*hs3	101 ± 2	1688 ± 62	102.9 ± 1.9	-125 ± 17	1.84
6b-4	236 ± 3	154 ± 13	90.1 ± 0.7	-1 ± 7	1.14
*hs1	120 ± 4	1271 ± 80	108.3 ± 2.7	-169 ± 21	1.39
hs2	121 ± 3	1248 ± 56	99.8 ± 1.8	-98 ± 16	1.52
6b-5	226 ± 3	203 ± 14	89.6 ± 0.7	5 ± 8	1.30
hs1	137 ± 3	980 ± 40	93.2 ± 1.4	-35 ± 14	1.72
hs2	136 ± 3	994 ± 51	90.2 ± 1.6	-3 ± 18	1.66
6b-6	216 ± 2	259 ± 14	89.9 ± 0.7	1 ± 7	1.23
hs1	145 ± 2	874 ± 26	94.4 ± 0.9	-47 ± 9	1.41
hs2	143 ± 3	898 ± 40	97.7 ± 1.3	-79 ± 12	1.16
6b-7	223 ± 3	221 ± 14	90.5 ± 0.7	-6 ± 7	1.01
hs1	100 ± 4	1720 ± 98	96.1 ± 2.2	-63 ± 21	0.99
6b-8	233 ± 3	167 ± 13	90.4 ± 0.7	-5 ± 7	1.55
hs1	140 ± 5	945 ± 70	87.1 ± 2.6	33 ± 31	2.51
hs2	135 ± 6	1013 ± 90	86.6 ± 2.8	39 ± 34	1.86
hs3	151 ± 3	807 ± 34	90.1 ± 1.1	-1 ± 12	1.50
6b-9	235 ± 3	156 ± 13	89.9 ± 0.7	1 ± 7	1.14
hs1	401 ± 12	-321 ± 20	88.9 ± 1.4	13 ± 16	2.35
hs2	140 ± 3	940 ± 44	88.4 ± 1.4	18 ± 16	1.64
hs3	138 ± 7	975 ± 100	94.0 ± 3.6	-43 ± 36	1.75
6b-10	211 ± 2	287 ± 14	90.5 ± 0.7	-6 ± 7	1.23
hs1	150 ± 6	818 ± 70	90.5 ± 1.7	-6 ± 19	0.87
hs2	148 ± 2	833 ± 23	94.4 ± 0.8	-47 ± 8	1.90
6b-11	239 ± 3	138 ± 13	90.1 ± 0.7	-1 ± 7	1.14
6b-12	228 ± 3	195 ± 13	90.1 ± 0.7	-1 ± 7	0.87
hs1	125 ± 3	1170 ± 55	96.6 ± 1.3	-68 ± 12	0.72
hs2	129 ± 7	1115 ± 108	96.0 ± 2.7	-62 ± 27	0.92

\* Hotspots with anomalous C isotopic compositions (data from [Floss and Stadermann, 2009b](#)); errors are  $1\sigma$  and are below 1‰ for all  $\text{CN}^-/\text{C}^-$  ratios; n.d. = not determined.

Table A2

Nitrogen and C isotopic compositions of matrix and hotspots in MET 00426.

Area	$^{14}\text{N}/^{15}\text{N}$	$\delta^{15}\text{N}$ (‰)	$^{12}\text{C}/^{13}\text{C}$	$\delta^{13}\text{C}$ (‰)	$\text{CN}^-/\text{C}^-$
1a-1	264 ± 4	29 ± 16	89.3 ± 0.9	8 ± 10	1.87
1a-2	260 ± 4	46 ± 17	89.2 ± 0.9	9 ± 10	1.53
hs1	171 ± 7	594 ± 69	91.2 ± 2.2	-13 ± 23	1.15
1a-3	262 ± 4	40 ± 16	89.7 ± 0.9	4 ± 10	1.09
hs1	367 ± 12	-259 ± 24	94.0 ± 1.8	-43 ± 18	2.58
1a-4	263 ± 4	35 ± 16	89.5 ± 0.9	6 ± 10	1.03
hs1	109 ± 4	1499 ± 84	89.3 ± 2.2	8 ± 25	1.45
hs2	142 ± 6	915 ± 79	92.6 ± 2.8	-28 ± 29	1.77
1a-5	271 ± 4	5 ± 16	89.7 ± 0.9	4 ± 10	0.97
1a-6	254 ± 4	70 ± 17	90.7 ± 0.9	-8 ± 10	1.65
hs1	136 ± 9	1007 ± 132	99.9 ± 4.4	-99 ± 40	1.39

(continued on next page)

Table A2 (continued)

Area	$^{14}\text{N}/^{15}\text{N}$	$\delta^{15}\text{N}$ (‰)	$^{12}\text{C}/^{13}\text{C}$	$\delta^{13}\text{C}$ (‰)	$\text{CN}^-/\text{C}^-$
hs2	169 ± 4	608 ± 39	92.1 ± 1.7	-23 ± 18	2.58
hs3	147 ± 3	856 ± 40	90.8 ± 1.3	-9 ± 14	1.71
1a-7	260 ± 4	46 ± 16	n.d.	n.d.	
1a-8	266 ± 4	24 ± 16	n.d.	n.d.	
hs1	146 ± 11	862 ± 134	n.d.	n.d.	
1a-9	273 ± 4	-5 ± 16	n.d.	n.d.	
1a-10	278 ± 4	-22 ± 16	n.d.	n.d.	
1a-11	272 ± 4	0 ± 16	n.d.	n.d.	
hs1	126 ± 3	1158 ± 57	n.d.	n.d.	
1a-12	270 ± 4	9 ± 16	90.0 ± 0.9	0 ± 10	0.99
hs1	156 ± 7	743 ± 75	90.5 ± 2.6	-6 ± 28	1.53
1a-13	271 ± 4	2 ± 16	90.0 ± 0.9	0 ± 10	0.93
hs1	178 ± 12	528 ± 104	87.0 ± 3.0	34 ± 35	0.99
1a-14	265 ± 4	27 ± 16	89.9 ± 0.9	1 ± 10	1.09
hs1	142 ± 8	917 ± 107	88.9 ± 4.2	15 ± 48	1.93
hs2	159 ± 7	711 ± 77	87.9 ± 3.2	24 ± 38	2.33
1a-15	258 ± 4	55 ± 17	90.2 ± 0.9	-3 ± 10	1.03
hs1	119 ± 4	1289 ± 72	96.2 ± 2.0	-64 ± 19	1.13
1a-16	257 ± 4	59 ± 17	90.3 ± 0.9	-4 ± 10	1.21
hs1	102 ± 3	1667 ± 78	95.9 ± 2.3	-61 ± 22	1.39
hs2	131 ± 5	1074 ± 74	92.3 ± 2.1	-25 ± 22	1.13
1a-17	262 ± 4	39 ± 16	90.2 ± 0.9	-3 ± 10	0.89
hs1	139 ± 5	956 ± 70	87.0 ± 2.0	34 ± 24	1.19
*hs2	356 ± 15	-236 ± 33	106.7 ± 3.2	-156 ± 25	2.72
1a-18	263 ± 4	34 ± 16	89.9 ± 0.9	2 ± 10	0.62
hs1	160 ± 9	701 ± 99	94.5 ± 4.1	-48 ± 41	1.65
1a-19	268 ± 4	16 ± 16	89.8 ± 0.9	3 ± 10	0.66
1a-20	269 ± 4	11 ± 16	89.8 ± 0.9	3 ± 10	0.56
1b-1	242 ± 4	122 ± 18	91.7 ± 0.9	-18 ± 10	2.03
hs1	141 ± 8	932 ± 114	88.4 ± 3.2	18 ± 37	1.31
hs2	133 ± 7	1047 ± 106	101.1 ± 4.1	-110 ± 36	2.09
1c-1	241 ± 4	127 ± 18	92.0 ± 0.9	-22 ± 10	2.21
hs1	129 ± 6	1105 ± 100	98.6 ± 3.1	-87 ± 28	1.29
1c-2	230 ± 4	185 ± 19	91.7 ± 0.9	-18 ± 10	1.77
hs1	87 ± 5	2124 ± 183	98.2 ± 3.7	-84 ± 35	0.87
hs2	106 ± 5	1555 ± 128	91.0 ± 4.5	-11 ± 49	2.49
1c-3	247 ± 4	103 ± 17	91.4 ± 0.9	-15 ± 10	1.67
1c-4	238 ± 4	144 ± 18	91.4 ± 0.9	-15 ± 10	1.77
hs1	123 ± 3	1218 ± 59	92.7 ± 1.7	-29 ± 18	1.49
5a-1	238 ± 4	142 ± 18	89.0 ± 0.9	12 ± 10	0.68
hs1	143 ± 5	908 ± 73	90.5 ± 1.8	-6 ± 20	0.74
5a-2	245 ± 4	109 ± 18	89.0 ± 0.9	12 ± 10	0.40
5a-3	257 ± 4	59 ± 17	89.7 ± 0.9	4 ± 10	1.17
hs1	136 ± 3	1002 ± 51	84.2 ± 1.0	69 ± 13	0.48
hs2	141 ± 6	925 ± 79	88.3 ± 2.3	19 ± 27	1.33
5a-4	268 ± 4	15 ± 17	89.1 ± 0.9	10 ± 10	0.60
5a-5	250 ± 4	89 ± 18	88.8 ± 0.9	14 ± 10	0.54
5a-6	217 ± 3	255 ± 20	89.9 ± 0.9	1 ± 10	0.64
hs1	130 ± 3	1100 ± 51	91.6 ± 1.1	-17 ± 12	0.48
hs2	131 ± 4	1072 ± 62	93.4 ± 1.2	-37 ± 12	0.30
hs3	136 ± 3	993 ± 50	89.3 ± 1.5	8 ± 17	2.13
5a-7	273 ± 4	-3 ± 16	90.3 ± 0.9	-4 ± 10	1.77
5a-8	225 ± 4	206 ± 19	88.0 ± 0.9	22 ± 10	0.70
hs1	430 ± 20	-367 ± 30	92.6 ± 2.0	-28 ± 21	1.63
5a-9	237 ± 4	146 ± 18	89.5 ± 0.9	6 ± 10	0.78
hs1	122 ± 7	1222 ± 129	85.9 ± 2.9	48 ± 35	1.05
5a-10	242 ± 4	126 ± 18	90.2 ± 0.9	-3 ± 10	1.39
hs1	151 ± 3	807 ± 41	92.4 ± 1.6	-26 ± 16	2.70
5a-11	219 ± 3	242 ± 20	n.d.	n.d.	
hs1	128 ± 4	1130 ± 56	n.d.	n.d.	
5b-1	229 ± 4	188 ± 19	90.0 ± 0.9	0 ± 10	0.76

(continued on next page)

Table A2 (continued)

Area	$^{14}\text{N}/^{15}\text{N}$	$\delta^{15}\text{N}$ (‰)	$^{12}\text{C}/^{13}\text{C}$	$\delta^{13}\text{C}$ (‰)	$\text{CN}^-/\text{C}^-$
hs1	152 ± 3	791 ± 34	91.5 ± 1.2	-16 ± 13	2.03
hs2	162 ± 6	681 ± 65	92.3 ± 1.7	-25 ± 18	0.74
5b-2	219 ± 3	242 ± 20	91.3 ± 0.9	-14 ± 10	0.72
hs1	136 ± 5	999 ± 67	91.0 ± 2.5	-11 ± 27	2.23
hs2	129 ± 5	1112 ± 78	93.2 ± 2.4	-34 ± 25	1.79
hs3	140 ± 7	937 ± 93	90.7 ± 2.0	-8 ± 22	0.64
5b-3	190 ± 3	430 ± 22	89.9 ± 0.9	2 ± 10	0.87
hs1	94 ± 3	1907 ± 89	95.9 ± 1.7	-61 ± 17	0.72
hs2	90 ± 3	2006 ± 91	94.3 ± 1.7	-46 ± 18	0.68
hs3	91 ± 2	1977 ± 69	94.5 ± 1.4	-48 ± 14	0.91
hs4	97 ± 2	1805 ± 59	93.9 ± 1.4	-42 ± 14	1.11
hs5	96 ± 4	1841 ± 108	98.3 ± 2.5	-84 ± 24	0.95
hs6	101 ± 2	1688 ± 66	96.9 ± 1.5	-71 ± 15	0.91
hs7	96 ± 2	1846 ± 64	93.9 ± 1.8	-42 ± 19	1.79
hs8	100 ± 2	1714 ± 54	92.6 ± 1.4	-28 ± 15	2.03
5b-4	219 ± 3	244 ± 19	90.1 ± 0.9	-2 ± 10	0.91
hs1	107 ± 4	1534 ± 95	92.6 ± 3.5	-28 ± 37	2.49
5b-5	211 ± 3	288 ± 20	90.7 ± 0.9	-8 ± 10	1.33
hs1	119 ± 2	1292 ± 47	90.6 ± 1.6	-7 ± 18	3.40
hs2	122 ± 3	1238 ± 58	94.4 ± 1.7	-47 ± 17	1.29
5b-6	232 ± 4	172 ± 19	89.8 ± 0.9	3 ± 10	0.66
hs1	145 ± 3	878 ± 36	94.6 ± 1.4	-49 ± 14	2.51
hs2	167 ± 8	630 ± 74	79.1 ± 1.0	138 ± 14	0.36
5b-7	192 ± 3	414 ± 22	90.4 ± 0.9	-5 ± 10	1.11
hs1	85 ± 1	2201 ± 55	99.9 ± 1.5	-99 ± 13	4.89
5b-8	222 ± 3	225 ± 19	91.2 ± 0.9	-13 ± 10	1.27
hs1	88 ± 2	2090 ± 54	96.9 ± 1.3	-71 ± 12	2.53
5b-9	230 ± 4	183 ± 19	90.5 ± 0.9	-6 ± 10	0.93
hs1	121 ± 3	1242 ± 52	87.5 ± 1.2	28 ± 14	0.91
5b-10	214 ± 3	270 ± 20	90.7 ± 0.9	-8 ± 10	0.99
hs1	370 ± 14	-266 ± 28	96.3 ± 2.3	-65 ± 23	2.98
hs2	129 ± 4	1101 ± 63	92.4 ± 1.9	-26 ± 20	1.39
6b-1	238 ± 4	144 ± 20	89.2 ± 0.9	9 ± 11	1.05
hs1	145 ± 6	875 ± 75	91.2 ± 2.1	-13 ± 22	0.99
6b-2	267 ± 4	20 ± 17	89.5 ± 0.9	6 ± 10	1.05
6b-3	264 ± 5	29 ± 21	89.1 ± 0.9	10 ± 11	0.38
6b-4	255 ± 4	66 ± 17	89.4 ± 0.9	7 ± 10	0.68
hs1	163 ± 4	672 ± 37	91.1 ± 1.5	-12 ± 16	2.17
6d-1	261 ± 4	42 ± 17	89.4 ± 0.9	7 ± 10	0.66
6d-2	188 ± 3	443 ± 23	86.9 ± 0.9	35 ± 10	0.78
hs1	132 ± 2	1056 ± 34	81.9 ± 0.8	99 ± 11	1.01
6d-3	251 ± 4	84 ± 18	n.d.	n.d.	
6d-4	268 ± 5	17 ± 20	n.d.	n.d.	
6d-5	257 ± 4	59 ± 18	n.d.	n.d.	
6d-6	212 ± 3	282 ± 20	n.d.	n.d.	
hs1	136 ± 2	1002 ± 36	n.d.	n.d.	
hs2	140 ± 3	943 ± 35	n.d.	n.d.	
6d-7	251 ± 4	86 ± 17	n.d.	n.d.	
6d-8	248 ± 4	96 ± 17	n.d.	n.d.	
6d-9	242 ± 4	122 ± 18	n.d.	n.d.	
hs1	429 ± 34	-366 ± 50	n.d.	n.d.	
6e-1	269 ± 4	10 ± 17	89.0 ± 0.9	12 ± 10	0.52
6e-2	217 ± 4	252 ± 20	90.1 ± 0.9	-2 ± 10	0.93
6e-3	277 ± 5	-17 ± 17	89.9 ± 0.9	2 ± 10	0.48
6e-4	268 ± 4	17 ± 16	89.9 ± 0.9	1 ± 10	0.60
6e-5	275 ± 4	-10 ± 16	90.2 ± 0.9	-3 ± 10	0.62
6e-6	247 ± 4	102 ± 18	89.9 ± 0.9	1 ± 10	0.54
hs1	121 ± 4	1252 ± 73	93.2 ± 2.2	-34 ± 22	1.35
6e-7	244 ± 4	116 ± 18	90.9 ± 0.9	-10 ± 10	0.89
hs1	1412 ± 7	919 ± 93	88.3 ± 2.1	19 ± 24	0.62
6e-8	237 ± 4	149 ± 18	90.3 ± 0.9	-4 ± 10	0.80

(continued on next page)

Table A2 (continued)

Area	$^{14}\text{N}/^{15}\text{N}$	$\delta^{15}\text{N}$ (‰)	$^{12}\text{C}/^{13}\text{C}$	$\delta^{13}\text{C}$ (‰)	$\text{CN}^-/\text{C}^-$
hs1	143 ± 6	908 ± 82	89.4 ± 1.9	7 ± 21	0.76
hs2	147 ± 4	848 ± 51	90.9 ± 1.6	−10 ± 17	1.29
hs3	152 ± 4	788 ± 42	91.6 ± 1.1	−17 ± 12	0.66
hs4	151 ± 3	798 ± 33	91.9 ± 1.0	−21 ± 11	1.13
6e-9	265 ± 4	28 ± 17	90.5 ± 0.9	−6 ± 10	0.76
6e-10	259 ± 4	48 ± 17	90.7 ± 0.9	−8 ± 10	0.80
hs1	157 ± 10	731 ± 105	86.0 ± 2.4	47 ± 29	0.76
hs2	157 ± 5	737 ± 51	90.8 ± 1.8	−9 ± 20	1.61
6e-11	275 ± 4	−9 ± 16	90.1 ± 0.9	−2 ± 10	0.60
6e-12	260 ± 4	46 ± 17	90.6 ± 0.9	−7 ± 10	0.93
hs1	106 ± 12	1559 ± 278	76.0 ± 5.7	184 ± 89	1.37

\* Hotspots with anomalous C isotopic compositions (data from Floss and Stadermann, 2009b); errors are  $1\sigma$  and are below 1% for all  $\text{CN}^-/\text{C}^-$  ratios; n.d. = not determined.

## REFERENCES

- Abreu N. and Brearley A. (2010) Early solar system processes recorded in the matrices of two highly pristine CR3 carbonaceous chondrites, MET 00426 and QUE 99177. *Geochim. Cosmochim. Acta* **74**, 1146–1171.
- Adande G. R. and Ziurys L. M. (2012) Millimeter-wave observations of CN and HNC and their  $^{15}\text{N}$  isotopologues: a new evaluation of the  $^{14}\text{N}/^{15}\text{N}$  ratio across the Galaxy. *Astrophys. J.* **744**(194), 115. <http://dx.doi.org/10.1088/0004-637X/744/194>.
- Aléon J. (2010) Multiple origins of nitrogen isotopic anomalies in meteorites and comets. *Astrophys. J.* **722**, 1342–1351.
- Aléon J., Engrand C., Robert F. and Chaussidon M. (2001) Clues to the origin of interplanetary dust particles from the isotopic study of their hydrogen-bearing phases. *Geochim. Cosmochim. Acta* **65**, 4399–4412.
- Aléon J., Robert F., Chaussidon M. and Marty B. (2003) Nitrogen isotopic composition of macromolecular organic matter in interplanetary dust particles. *Geochim. Cosmochim. Acta* **67**, 3773–3787.
- Alexander C. M. O'D., Fogel M., Yabuta H. and Cody G. D. (2007) The origin and evolution of chondrites recorded in the elemental and isotopic compositions of their macromolecular organic matter. *Geochim. Cosmochim. Acta* **71**, 4380–4403.
- Alexander C. M. O'D., Newsome S. D., Fogel M. L., Nittler L. R., Busemann H. and Cody G. D. (2010) Deuterium enrichments in chondritic macromolecular material – implications for the origin and evolution of organics, water and asteroids. *Geochim. Cosmochim. Acta* **74**, 4417–4437.
- Bernstein M. P., Elsila J. E., Dworkin J. P., Sandford S. A., Allamandola L. J. and Zare R. N. (2002) Side group addition to the polycyclic aromatic hydrocarbon coronene by ultraviolet photolysis in cosmic ice analogs. *Astrophys. J.* **376**, 1115–1120.
- Bernstein M. P., Moore M. H., Elsila J. E., Sandford S. A., Allamandola L. J. and Zare R. N. (2003) Side group addition to the polycyclic aromatic hydrocarbon coronene by proton irradiation in cosmic ice analogs. *Astrophys. J.* **582**, L25–L29.
- Bonal L., Huss G. R., Krot A. N., Nagashima K., Ishii H. and Bradley J. P. (2010) Highly  $^{15}\text{N}$ -enriched chondritic clasts in the CB/CH-like meteorite Isheyevo. *Geochim. Cosmochim. Acta* **74**, 6590–6609.
- Bonal L., Alexander C. M. O'D., Huss G. R., Nagashima K., Quirico E. and Beck P. (2013) Hydrogen isotopic composition of water in CR chondrites. *Geochim. Cosmochim. Acta* **106**, 111–133.
- Brearley A. J. (1993) Matrix and fine-grained rims in the unequilibrated CO3 chondrite, ALHA77307: origins and evidence for diverse, primitive nebular dust components. *Geochim. Cosmochim. Acta* **57**, 1521–1550.
- Briani G., Gounelle M., Marrocchi Y., Mostefaoui S., Leroux H., Quirico E. and Meibom A. (2009) Pristine extraterrestrial material with unprecedented nitrogen isotopic variation. *Proc. Nat. Acad. Sci. U.S.A.* **106**, 10522–10527.
- Busemann H., Young A. F., Alexander C. M. O'D., Hoppe P., Mukhopadhyay S. and Nittler L. R. (2006) Interstellar chemistry recorded in organic matter from primitive meteorites. *Science* **312**, 727–730.
- Busemann H., Nguyen A. N., Cody G. D., Hoppe P., Kilcoyne A. L. D., Stroud R. M., Zega T. J. and Nittler L. R. (2009) Ultra-primitive interplanetary dust particles from the comet 26P/Grigg-Skjellerup dust stream collection. *Earth Planet. Sci. Lett.* **288**, 44–57.
- Chakraborty S., Jackson T. L., Muskatel B. H., Ahmed M., Levine R. D. and Thieme M. H. (2013) Huge isotopic effect in VUV photodissociation of  $\text{N}_2$ : implications for meteorite data. *Lunar Planet. Sci. XLIV*. Lunar Planet. Inst, Houston. #1043 (abstr.).
- Ciesla F. J. and Sandford S. A. (2012) Organic synthesis via irradiation and warming of ice grains in the solar nebula. *Science* **336**, 452–454.
- Clayton R. N. (2002) Self-shielding in the solar nebula. *Nature* **415**, 860–861.
- Cody G. D. and Alexander C. M. O'D. (2005) NMR studies of structural variation of insoluble organic matter from different carbonaceous chondrite groups. *Geochim. Cosmochim. Acta* **69**, 1085–1097.
- Cody G. D., Ade H., Alexander C. M. O'D., Araki T., Butterworth A., Fleckenstein H., Flynn G., Gilles M. K., Jacobsen C., Kilcoyne A. L. D., Messenger K., Sandford S. A., Tyliczszak T., Westphal A. J., Wirick S. and Yabuta H. (2008) Quantitative organic and light-element analysis of comet 81P/Wild 2 particles using C-, N-, and O- $\mu$ -XANES. *Meteorit. Planet. Sci.* **43**, 353–365.
- De Gregorio B. T., Stroud R. M., Nittler L. R., Alexander C. M. O'D., Bassim N. D., Cody G. D., Kilcoyne A. L. D., Sandford S. A., Milam S. N., Nuevo M. and Zega T. J. (2013) Isotopic and chemical variation of organic nanoglobules in primitive meteorites. *Meteorit. Planet. Sci.* **48**, 904–928.
- Derenne S. and Robert F. (2010) Model of molecular structure of the insoluble organic matter isolated from Murchison meteorite. *Meteorit. Planet. Sci.* **45**, 1461–1475.
- Floss C. and Stadermann F. J. (2005) Presolar (circumstellar and interstellar) phases in Renazzo: the effects of parent body processing. *Lunar Planet. Sci. XXXVI*. Lunar Planet. Inst, Houston. #1390 (abstr.).

- Floss C. and Stadermann F. J. (2009a) Auger Nanoprobe analysis of presolar ferromagnesian silicate grains from primitive CR chondrites QUE 99177 and MET 00426. *Geochim. Cosmochim. Acta* **73**, 2415–2440.
- Floss C. and Stadermann F. J. (2009b) High abundances of circumstellar and interstellar C-anomalous phases in the primitive CR3 chondrites QUE 99177 and MET 00426. *Astrophys. J.* **697**, 1242–1255.
- Floss C. and Stadermann F. J. (2009c) Interstellar components in the primitive CR3 chondrites QUE 99177 and MET 00426. *Lunar Planet. Sci. XL*. Lunar Planet. Inst, Houston. #1083 (abstr.).
- Floss C., Stadermann F. J., Bradley J., Dai Z., Bajt S. and Graham G. (2004) Carbon and nitrogen isotopic anomalies in an anhydrous interplanetary dust particle. *Science* **303**, 1355–1358.
- Floss C., Stadermann F. J., Bradley J. P., Dai Z. R., Bajt S., Graham G. and Lea A. S. (2006) Identification of isotopically primitive interplanetary dust particles: a NanoSIMS isotopic imaging study. *Geochim. Cosmochim. Acta* **70**, 2371–2399.
- Floss C., Stadermann F. J., Mertz A. F. and Bernatowicz T. (2010) A NanoSIMS and Auger Nanoprobe investigation of an isotopically primitive interplanetary dust particle from the 55P/Tempel-Tuttle targeted stratospheric dust collector. *Meteorit. Planet. Sci.* **45**, 1889–1905.
- Floss C., Le Guillou C., Stadermann F. J. and Brearley A. (2011) Coordinated NanoSIMS and TEM analyses of C- and N-anomalous phases in the CR3 chondrite MET 00426. *Lunar Planet. Sci. XLII*. Lunar Planet. Inst, Houston. #1455 (abstr.).
- Füri E., Aléon-Toppa A., Marty B., Libourel G. and Zimmermann L. (2013) Effects of atmospheric entry heating on the noble gas and nitrogen content of micrometeorites. *Earth Planet. Sci. Lett.* **377–378**, 1–12.
- Garvie L. A. J., Baumgardner G. and Buseck P. R. (2008) Scanning electron microscopical and cross sectional analysis of extraterrestrial carbonaceous nanoglobules. *Meteorit. Planet. Sci.* **43**, 899–903.
- Glavin D. P., Callahan M. P., Dworkin J. P. and Elsila J. E. (2011) The effects of parent body processes on amino acids in carbonaceous chondrites. *Meteorit. Planet. Sci.* **45**, 1948–1972.
- Gourier D., Robert F., Delpoux O., Binet L., Vezin H., Moissette A. and Derenne S. (2008) Extreme deuterium enrichment of organic radicals in the Orgueil meteorite: revisiting the interstellar interpretation. *Geochim. Cosmochim. Acta* **72**, 1914–1923.
- Greshake A. (1997) The primitive matrix components of the unique carbonaceous chondrite Acfer 094: a TEM study. *Geochim. Cosmochim. Acta* **61**, 437–452.
- Harrington R. and Righter K. (2013) Carbonaceous chondrite thin section preparation. *Lunar Planet. Sci. XLIV*. Lunar Planet. Inst, Houston. #2206 (abstr.).
- Hashigushi M., Kobayashi S. and Yurimoto H. (2013) In situ observation of D-rich carbonaceous globules embedded in NWA 801 CR2 chondrite. *Geochim. Cosmochim. Acta* **122**, 306–323.
- Hashizume K., Takahata N., Naraoka H. and Sano Y. (2011) Extreme oxygen isotope anomaly with a solar origin detected in meteoritic organics. *Nature Geosci.* **4**. <http://dx.doi.org/10.1038/NCEO1070>.
- Hayes J. M., Kaplan I. R. and Wedeking K. W. (1983) Precambrian organic geochemistry, preservation of the record. In *Earth's earliest biosphere: its origin and evolution* (ed. J. W. Schopf). Princeton University, Princeton, NJ, pp. 93–134.
- Herd C. D. K., Sharp Z. D., Alexander C. M. O'D. and Blinova A. (2012) Oxygen isotopic composition of Tagish Lake lithologies: insights into parent body alteration. *Lunar Planet. Sci. XLIII*. Lunar Planet. Inst, Houston. #1688 (abstr.).
- Hily-Blant P., Bonal L., Faure A. and Quirico E. (2013) The <sup>15</sup>N-enrichment in dark clouds and solar system objects. *Icarus* **223**, 582–590.
- Krot A. N., Meibom A., Weisberg M. K. and Keil K. (2002) The CR chondrite clan: implications for early solar system processes. *Meteorit. Planet. Sci.* **37**, 1451–1490.
- Le Guillou C. and Brearley A. J. (2013) Relationships between organics, water and early stages of aqueous alteration in the pristine CR3.0 chondrite MET 00426. *Geochim. Cosmochim. Acta*, in press, <http://dx.doi.org/10.1016/j.gca.2013.10.024>.
- Le Guillou C., Brearley A. J., Floss C. and Stadermann F. J. (2010) In situ observation of C and N anomalous organic grains in the matrix of MET 00426. *Meteorit. Planet. Sci.* **45**, A71 (abstr.).
- Le Guillou C., Rouzaud J.-N., Bonal L., Quirico E., Derenne S. and Remusat L. (2012) High resolution TEM of chondritic carbonaceous matter: metamorphic evolution and heterogeneity. *Meteorit. Planet. Sci.* **47**, 345–362.
- Le Guillou C., Bernard S., Brearley A. J. and Remusat L. (in press) Evolution of organic matter in Orgueil, Murchison and Renazzo during parent body aqueous alteration: in-situ investigations. *Geochim. Cosmochim. Acta*, doi: <http://dx.doi.org/10.1016/j.gca.2013.11.020>.
- Lyons J. R., Bergin E. A., Ciesla F. J., Davis A. M., Desch S. J., Hashizume K. and Lee J.-E. (2009) Timescales for the evolution of oxygen isotope compositions in the solar nebula. *Geochim. Cosmochim. Acta* **73**, 4998–5017.
- Martins Z., Alexander C. M. O'D., Orzechowska G. E., Elsila J. E., Glavin J. P., Dworkin J. P., Septhorn M. A. and Ehrenfreund P. (2008) Amino acid composition of primitive CR2 chondrites. *Meteorit. Planet. Sci.* **43**, A90.
- Messenger S. and Keller L. P. (2005) Association of presolar grains with molecular cloud material in IDPs. *Lunar Planet. Sci. XXXVI*. Lunar Planet. Inst, Houston. #1846 (abstr.).
- Messenger S. and Walker R. M. (1997) Evidence for molecular cloud material in meteorites and interplanetary dust. In *Astrophysical Implications of the Laboratory Study of Presolar Materials*, vol. 402 (eds. T. Bernatowicz and E. Zinner). AIP Conference Proc. pp. 545–564.
- Messenger S., Stadermann F. J., Floss C., Nittler L. R. and Mukhopadhyay S. (2003) Isotopic signatures of presolar materials in interplanetary dust. *Space Sci. Rev.* **106**, 155–172.
- Nagashima K., Krot A. N. and Yurimoto H. (2004) Stardust silicates from primitive meteorites. *Nature* **428**, 921–924.
- Nakamura-Messenger K., Messenger S., Keller L. P., Clemett S. J. and Zolensky M. E. (2006) Organic globules in the Tagish Lake meteorite: remnants of the protosolar disk. *Science* **314**, 1439–1442.
- Nguyen A. N., Nittler L., Stadermann F. J., Stroud R. and Alexander C. M. O'D. (2010) Coordinated analyses of presolar grains in the Allan Hills 77307 and Queen Elizabeth Range 99177 meteorites. *Astrophys. J.* **719**, 166–189.
- Pizzarello S. and Holmes W. (2009) Nitrogen-containing compounds in two CR2 meteorites: <sup>15</sup>N composition, molecular distribution and precursor molecules. *Geochim. Cosmochim. Acta* **73**, 2150–2162.
- Remusat L., Palhol F., Robert F., Derenne S. and France-Lanord C. (2006) Enrichment of deuterium in insoluble organic matter from primitive meteorites: a solar system origin? *Earth Planet. Sci. Lett.* **243**, 15–25.
- Remusat L., Meibom A., Mostefaoui S., Delpoux O., Binet L., Gourier D. and Derenne S. (2009) Proto-planetary disk chemistry recorded by D-rich organic radicals in carbonaceous chondrites. *Astrophys. J.* **698**, 2087–2092.
- Remusat L., Guan Y., Wang Y. and Eiler J. M. (2010) Accretion and preservation of D-rich organic particles in carbonaceous

- chondrites: evidence for important transport in the early solar nebula. *Astrophys. J.* **713**, 1048–1058.
- Rodgers S. D. and Charnley S. B. (2008) Nitrogen superfractionation in dense cloud cores. *Mon. Not. R. Astron. Soc.* **385**, L48–L52.
- Sephton M. A., Verchovsky A. B., Bland P. A., Gilmour I., Grady M. M. and Wright I. P. (2003) Investigating the variations in carbon and nitrogen isotopes in carbonaceous chondrites. *Geochim. Cosmochim. Acta* **67**, 2093–2108.
- Stadermann F. J., Croat T. K., Bernatowicz T. J., Amari S., Messenger S., Walker R. M. and Zinner E. (2005) Supernova graphite in the NanoSIMS: carbon, oxygen and titanium isotopic compositions of a spherule and its TiC sub-components. *Geochim. Cosmochim. Acta* **69**, 177–188.
- Stadermann F. J., Floss C., Bose M. and Lea A. S. (2009) The use of Auger spectroscopy for the in situ elemental characterization of sub-micrometer presolar grains. *Meteorit. Planet. Sci.* **44**, 1033–1049.
- Terzieva R. and Herbst E. (2000) The possibility of nitrogen isotopic fractionation in interstellar clouds. *Mon. Not. R. Astron. Soc.* **317**, 563–568.
- Wirström E. S., Charnley S. B., Cordiner M. A. and Milam S. N. (2012) Isotopic anomalies in primitive solar system matter: spin-state dependent fractionation of nitrogen and deuterium in interstellar clouds. *Astrophys. J.* **757**(L11), 15. <http://dx.doi.org/10.1088/2041-8205/757/L11>.

Associate editor: Trevor Ireland